Probing the deep mantle wedge in an active subduction zone: Xenoliths from the Mercaderes Volcanic District, Southern Colombia

Luca Notini, Marco Scambelluri, Andrea Tommasi, Alberto Zanetti, Fabio Ferri, A. Rodríguez-Vargas, Elisabetta Rampone

This is an author copy of the final revised article published in Lithos in October 2023
For citation please refer to the published version:
Notini L., Scambelluri M., Tommasi, A., Zanetti A., Ferri F., Rodríguez-Vargas A., Rampone E. Probing the deep mantle wedge in an active subduction zone: Mantle xenoliths from the Mercaderes Volcanic District, Southern Colombia Lithos, 464-465 (2024) 107401,
doi: 10.1016/j.lithos.2023.107401

Probing the deep mantle wedge in an active subduction zone: Xenoliths from the Mercaderes Volcanic District, Southern Colombia

L. Notini [a], M. Scambelluri [a,*], A. Tommasi [b], A. Zanetti [c], F. Ferri [d], A. Rodríguez-Vargas [e], E. Rampone [a]

[a] *Dipartimento di Scienze della Terra, dell'Ambiente e della Vita, Università di Genova, Genova, Italy*
[b] *Géosciences Montpellier, CNRS and Université de Montpellier, France*
[c] *IGG-CNR Pavia, Pavia, Italy*
[d] *Dipartimento di Geoscienze, Università di Padova, Padova, Italy*
[e] *Minerlab, Bogotà, Colombia*

ARTICLE INFO

Keywords:
Mantle wedge
Subduction zones
Garnet-bearing mantle peridotite
Garnet-bearing mantle pyroxenite
Metasomatism

ABSTRACT

In subduction zones, the mantle wedge is the domain where liquid phases released by the oceanic subducting plates cause mantle hydration, metasomatism, and partial melting, producting the arc crust. However, direct petrologic information on mantle wedges overlying active subduction zones remains scarce. Here we constrain key aspects of the petrological evolution of the supra-subduction mantle underneath the active volcanic district of Southern Colombia (Mercaderes) by studying a unique suite of peridotite and pyroxenite xenoliths hosted by andesites and lamprophyres. These garnet-bearing peridotite, websterite, clino- and orthopyroxenite xenoliths equilibrated between 2.5 and 4 GPa and 1100–1200 °C. The studied rocks display considerable heterogeneity in terms of lithotypes, textures, mineral abundance and extent of metasomatic overprint. Most samples display fine-grained mylonitic textures overprinting coarse-grained peridotite and garnet pyroxenite precursors; the EBSD study of undeformed garnet websterite samples suggests crystallization from melts and/or melt-rock reaction processes. Modal enrichment in clinopyroxene as well as in the alkalis and LREE contents in some garnet peridotite implies interaction with alkaline basaltic melts, whereas enrichment in silica, Pb and Sr in the garnet-bearing orthopyroxenites records interaction with metasomatic, slab-derived liquids. Some garnet clinopyroxenite xenoliths display marked positive Sr anomalies and minor Eu anomalies, indicating derivation of these rocks from Mg-rich, plagioclase-bearing (and garnet-absent) low-pressure cumulates. Their equilibration in the garnet field implies that after crystallization these clinopyroxenites were transported to deeper levels in the mantle, as the result of foundering into the mantle of the dense arc roots, as already documented in Mercaderes and elsewhere in the Andes. In conclusion, the Mercaderes xenoliths probe a heterogeneous and chemically active domain of the Colombian mantle wedge, where deep sinking lower crustal rocks, melt metasomatism by distinct venues of chemically different melts, and deformation predate fast exhumation by volatile-rich melts.

1. Introduction

Subduction zones are highly dynamic environments where burial of hydrated and carbonated oceanic plates releases aqueous-carbonic fluids and melts to the mantle. Fluid/melt migration out of the production sites triggers mantle metasomatism and melting (Stern, 2002; Tatsumi and Stern, 2006), thus concurring to major global processes such as arc magmatism, the creation of new continental crust and atmosphere evolution (Cartigny and Marty, 2013; Dasgupta, 2013).

The supra subduction mantle, also known as the mantle wedge, plays a key role in subduction dynamics. This domain of asthenospheric mantle accommodates the viscous deformation between the descending slab and the overriding plate (van Keken, 2003) and its metasomatism by slab agents and consequent melting is the prime cause of magmatism at convergent plate margins (Grove et al., 2006; Tatsumi et al., 1983; van Keken, 2003). However, direct study of the petrological processes

* Corresponding author.
E-mail addresses: luca.notini@edu.unige.it (L. Notini), marco.scambelluri@unige.it (M. Scambelluri), andrea.tommasi@umontpellier.fr (A. Tommasi), zanetti@crystal.unipv.it (A. Zanetti), fabio.ferri@eitrawmaterials.eu (F. Ferri), arodriguez@minerlablimitada.com (A. Rodríguez-Vargas), elisabetta.rampone@unige.it (E. Rampone).

https://doi.org/10.1016/j.lithos.2023.107401

occurring in the mantle wedge is limited by the paucity of rocks exhumed from such environments.

There are two major categories of mantle samples from subduction environments: (i) high-pressure orogenic peridotites and (ii) xenoliths carried by arc lavas. High-pressure orogenic peridotites are metasomatized spinel and garnet peridotites derived from cold domains of the supra-subduction mantle in contact with, or in proximity of, the subducting slab (Bodinier and Godard, 2003), which became tectonically scraped off their original supra-subduction domains and were exhumed to the surface in subduction channels (Brueckner and Medaris, 2000; Scambelluri et al., 2010). Known examples are mostly garnet peridotites, among which those from the Alpine Ulten Zone (Godard et al., 1996; Gudelius et al., 2019; Ionov et al., 2017; Pellegrino et al., 2021; Rampone and Morten, 2001; Sapienza et al., 2009; Scambelluri et al., 2006; Tumiati et al., 2003), Sulu in China (Malaspina et al., 2009, 2012; Zheng et al., 2005, 2008), and from Bardane, Fjørtoft island, Western Norway (Scambelluri et al., 2008; Van Roermund and Drury, 1998, Van Roermund et al., 2002). These rocks commonly contain hydrated minerals (amphibole, phlogopite) coexisting with garnet as the result of reactions with metasomatic slab fluids or melts at temperatures around 800–850 °C, as shown by thermobarometry of the above rock occurrences. In contrast, most of the mantle wedge xenolith occurrences described in literature are equilibrated at spinel-facies conditions at temperatures around 1000 °C, suggesting that they were extracted from the lithospheric mantle of the overriding plate (e.g., Arai and Ishimaru, 2008; Bertotto et al., 2013; Comin-Chiaramonti et al., 2001; Grégoire et al., 2001; Laurora et al., 2001; McInnes et al., 2001; Ponce et al., 2015; Rivalenti et al., 2000, 2004, 2007; ; Soustelle et al., 2010). Garnet-bearing supra-subduction mantle xenoliths are much rarer and mostly derive from back-arc settings (i.e., Dantas, 2007; Zaffarana et al., 2014). The asthenospheric domain of the supra subduction mantle wedge is the least sampled environment in subduction zones.

Here we present petrological data for rare garnet-bearing peridotite and pyroxenite xenoliths sampling the deep mantle wedge of an active subduction zone. These xenoliths were collected in the volcanic area of Mercaderes (Southern Colombia), which overlies the active subduction of the Nazca plate. The Mercaderes volcanics host a heterogeneous xenolith suite sampling the whole sequence underneath the volcano (from the deep mantle to crustal roots), including crustal rocks that foundered and re-equilibrated at mantle depths (Bloch et al., 2017; Weber, 1998; Weber et al., 2002; Zieman et al., 2023). Earlier studies of xenoliths from this area provide a description of the entire suite (Bloch et al., 2017; Rodriguez-Vargas et al., 2005; Weber, 1998; Weber et al., 2002), data on the Sr and Nd isotopic composition of garnet- and spinel-bearing peridotites and pyroxenites (Rodriguez-Vargas et al., 2005). Lu—Hf isotope ages of 4.2–4.5 Ma for the deep recrystallization of crustal xenoliths (Bloch et al., 2017) and the U—Pb dating at 238 (±19) ka (Zieman et al., 2023) of zircon from the host tuffs indicate that the Mercaderes xenoliths record recent stages of the sub-arc mantle evolution. The present study focuses on the petrology of garnet pyroxenite and peridotite xenoliths. We analyse the textures, major and trace element composition of the rock-forming minerals, and geothermobarometry data from this xenolith suite to characterize petrological processes active in the deep wedge mantle from an active subduction zone.

2. Geological and petrological context

The garnet-bearing mantle xenoliths presented here pertain to the Granatifera Tuff, a small tuff cone in the Mercaderes plateau (Southern Colombia), 1000 to 2000 m above sea level and made of numerous volcanic and volcano-sedimentary flows overlying Tertiary to Cretaceous metamorphic and sedimentary bedrocks. The Mercaderes district of the Andean Northern Volcanic Zone (NVZ) is west of the Central Cordillera of Northern Andes (Fig. 1A, B; coordinates: 1°40′ - 1°52′ northern latitude and 77°5′ - 77°20′ eastern longitude; Weber, 1998). The NVZ extends from central Colombia to central Ecuador for about 550 km. In agreement with previous authors (Pardo et al., 2019;

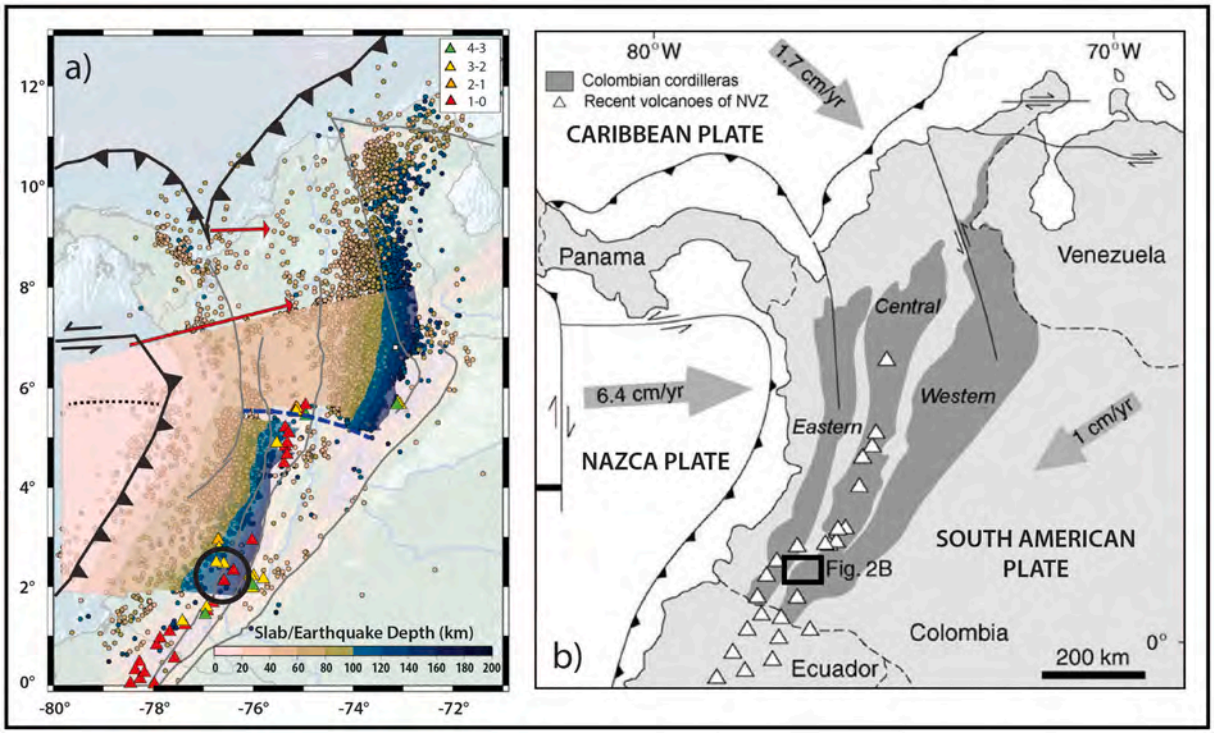

Fig. 1. (a) Recent geodynamic model of the area below Mercaderes (highlighted by the black circle) that locates the Nazca slab depth in the region, based on the position of the Wadati-Benioff plane (modified after Wagner et al., 2017). (b) Gedynamic setting of the region of interest, the position of the Mercaderes area in the Andean arc is highlighted by the black box.

Rodriguez-Vargas et al., 2005; Weber, 1998) we adopt the term "Granatífera Tuff" to define the lithostratigraphic units related to the volcanism sourced in the Mercaderes area, as the term "Mercaderes tuff" in literature is linked to the Ánimas volcano, that is unrelated to the Mercaderes volcanism.

The north-western corner of South America is a complex setting that accomplishes convergence between the South American, Nazca, and Caribbean plates. Recent studies document that, in western Colombia, between ~ 6 and 8°N, the subducting plate is fragmented in four main slab segments and one overlapping segment (e.g., Mojica Boada et al., 2022; Sun et al., 2022). Based on the pattern and age of the volcanic activity, Wagner et al. (2017) and Sun et al. (2022) proposed, from north to south, the following slab segments: (i) the Maracaibo slab, of Caribbean origin, subducting south of the Panama indenter (~8°N); (ii) the Bucaramanga and Medellín slabs, of Nazca or Caribbean origin, overlapping between ~8°N and ~5.5°N, delimited to the south by the Caldas tear; (iii) the Cartago and Pasto slabs, of Nazca origin, separated by the Malpelo tear. In contrast, Blanco et al. (2017) proposed that the upper plate in this area has a homogeneous lithospheric thickness between 100 and 110 km. The Mercaderes volcanism took place above the southernmost Pasto slab segment, whose dip is reasonably well constrained by models; the upper surface of the slab is located at 140–160 km depth beneath the sampling area (Mojica Boada et al., 2022). The age of the volcanic activity in Mercaderes spans from late Cenozoic to Pleistocene; ash bed zircon grains from the Granatifera Tuff were dated to ca. 240 ka using zircon U—Pb (Zieman et al., 2023).

Here we refer to the lithostratigraphic description and subdivision of the Granatifera Tuff by Rodriguez-Vargas et al. (2005) who identified three units: (1) the basal Unit A (200 m thick) consisting of alternating breccias and lapilli tuffs: the breccias contain clasts of andesite, schists and quartzite while the tuffs contain clasts of porphyritic andesite, diorite, smaller amounts of quartzite, schists, amphibolite, garnet granulite, pyroxenite and peridotite in an ash matrix; (2) the intermediate Unit B, <45 m thick, containing black and green schists, quartzites, amphibolites, gneisses, hornblendites, pyroxenites, and andesites; (3) the top Unit C, at the top, 50 m thick, comprising ash material (5 m), debris flow (40 m), and tuffs (5 m), with clasts of diabase, andesite, schists, quartzites, and pumice, which are <1 m in size. In addition to mantle (garnet-bearing peridotites and pyroxenites) and crustal (diorite, granulite, hornblendite) xenoliths, the Units A and B of the Granatifera Tuff also contains igneous xenoliths (volcanic fragments and bombs of dacitic, andesitic and lamprophyric compositions;Rodriguez-Vargas et al., 2005 ; Weber, 1998 ; Weber et al., 2002). Mantle xenoliths are also recovered in breccias inside lamprophyre and andesite fragments and bombs, that have been proposed as main original host for these rocks (Weber, 1998). Lamprophyres have a porphyritic texture with amphibole phenocrystals in a groundmass of plagioclase, amphibole, and pyroxene, while andesites are massive with phenocrystals of plagioclase and amphibole in a plagioclase, amphibole and pyroxene groundmass (Rodriguez-Vargas et al., 2005; Weber et al., 2002; Weber, 1998). Some contacts between xenoliths and the host lava are rimmed by nepheline aggregates formed as a product of interaction between rock and melt (Rodriguez-Vargas et al., 2005). The geochemistry of the andesite host rocks suggests an origin from partial melting of a mantle source whose isotopic signature is comparable to that of continental plateau basalts, while the lamprophyres derive from mantle wedge sources contaminated by a subduction component (Rodriguez-Vargas et al., 2005; Weber, 1998). The juvenile lava bombs within the pyroclastic flows hosting xenoliths, are basalts to basaltic andesites whose geochemical signature is indicative of primary or near-primary magmas (Grohn and Ibañe-Mejía, 2018; Pardo, personal communication).

The Mercaderes mantle xenoliths are mainly garnet-bearing peridotites and pyroxenites, with subordinated spinel-bearing peridotites. They have been described by Weber (1998) and Rodriguez-Vargas et al. (2005) as hydrous garnet-bearing websterites and lherzolites with dominant protogranular textures and subordinated porphyroclastic textures. The modal composition is dominated by clino- and orthopyroxene (Cr-diopside and enstatite), garnet (Cr-pyrope), with variable contents of olivine ($Fo_{89–92}$) and subordinate Cr-spinel, with kelyphytic rims (amphibole, spinel, pyroxenes, serpentine) around pyroxenes and olivine attributed to fluid percolation (Rodriguez-Vargas et al., 2005; Weber, 1998). Using the Brey and Köhler (1990) geothermometer and geobarometer, Weber (1998) proposed pressure-temperature estimates between 1100 and 1300 °C and 2.7–4.0 GPa for the garnet-bearing xenoliths and of 1.5 GPa and 1100 °C for the spinel-bearing xenoliths. The detailed thermobarometric study by Zieman et al. (2023) shows that the Mercaderes garnet peridotites display a bimodal distribution, with a group of xenoliths recording conditions of ~ 3 GPa and 1260–1290 °C and another group at 3.5-GPa and 1140–1230 °C, interpreted as convecting and cooler near-slab mantle domains, respectively. Weber (1998) also described carbonated mantle xenoliths that have been poorly investigated so far. These xenoliths contain secondary calcite, dolomite and aragonite possibly generated by metasomatic interaction of the silicate mantle assemblages with carbonic agents released by the subducting slab (Ferri et al., 2017).

Crustal xenoliths are predominantly hornblendite, pyroxenite, granulite, amphibolite, and subordinated orthogneiss (Gianola et al., 2023; Zieman et al., 2023; Bloch et al., 2017; Rodriguez-Vargas et al., 2005; Weber et al., 2002; Weber, 1998). Weber (1998) provided for the above rocks pressure-temperature estimates of 600–1000 °C and 1.0–1.5 GPa and suggested that the different xenolith types coexisted in the lower crust at the time of entrainment (Weber et al., 2002). Zieman et al. (2023) obtained for the 'crustal section' underneath Mercaderes pressure-temperature values of 1.2–2.2 GPa and 920–1280 °C and suggested that part of the deep crust and mantle underneath Mercaderes (mafic crust and pyroxenite) were in a partially molten state. Presence of partial melts in the arc roots of Mercaderes was confirmed by the observation of arclogite xenoliths hosting andesitic to rhyolitic primary melt inclusions in garnet, which suggest that differentiation of mantle-derived melts and lower crustal anatexis occurred in close association (Gianola et al., 2023). The above results agree with the estimates by Bloch et al. (2017) who obtained temperatures between 1050 and 1300 °C on crustal pyroxenites, according to the calibration by Ganguly et al. (1996) and pressures between 1.5 and 2.2 GPa based on the calibration by Beyer et al. (2015). Based on the rock compositions and on the above set of pressure-temperature estimates, Bloch et al. (2017) proposed that part of the Mercaderes xenoliths record recent delamination and foundering of the crustal arc root, a gravitational process that has been proposed for the Central Andes based on geodynamical models (Currie et al., 2015). According to Lu—Hf dating the crustal xenoliths are younger than 5 Ma (Bloch et al., 2017). However, foundering of the Mercaderes arc root may have been hampered by the diffuse occurrence of melts, which would decrease the bulk density of the lithosphere (Zieman et al., 2023; Gianola et al., 2023).

3. Samples and methods

The studied xenoliths show heterogenous textures and mineral assemblages. They can be classified in five categories (see Table 1): (1) porphyroclastic garnet and spinel peridotites, (2) coarse granular garnet websterites, (3) porphyroclastic garnet clinopyroxenites, (4) porphyroclatsic garnet orthopyroxenites, and (5) porphyroclastic websterites. All xenoliths are garnet-bearing except for a spinel lherzolite (sample 18XM5) and a websterite without garnet or spinel (sample 18XM7).

3.1. Electron microprobe

Major element analyses of all mineral phases and elemental maps were performed at the University of Milan (Electron microscope laboratory at *Dipartimento di Scienze della Terra "Ardito Desio"*) using a JEOL JXA 8200 electron microprobe equipped with wavelength dispersive spectrometers. All point analyses and the elemental maps have been

Table 1
Texture, modal composition and P-T equilibration conditions of the studied samples.

Sample	Rock type and texture	Modal composition volume %							T °C	P GPa
		Ol	Opx	Cpx	Grt	Sp	Phl	Parg		
18XM4	Porphyroclastic Grt peridotite	57	12	23	8	< 1	0	< 1	1150–1200	3.4–3.8
18XM12	Porphyroclastic Grt peridotite	62	19	11	8	< 1	0	< 1	1150–1200	3.0–3.5
18XM5	Porphyroclastic Sp peridotite	49	44	6	0	< 1	< 1	< 1	1100–1190	2.2. – 2.5
COL1	Coarse-granular Grt websterite	0	65	24	10	< 1	0	< 1	1190–1220	3.0–3.3
COL2	Coarse-granular Grt websterite	0	22	38	37	< 1	0	3	1170–1230	2.8–3.4
18XM6	Porphyroclastic Grt clinopyroxenite	0	< 1	52	44	< 1	0	3	990–1140	3.0–3.7
18XM9	Porphyroclastic Grt clinopyroxenite	0	< 1	36	63	0	0	< 1	1000–1100	2.4–3.3
18XM11	Porphyroclastic Grt clinopyroxenite	0	< 1	57	42	< 1	0	1	1000–1100	2.4–3.0
18XM2	Porphyroclastic Grt orthopyroxenite	0	88	2	10	< 1	0	< 1	1100–1210	2.7–4.0
18XM3	Porphyroclastic Grt orthopyroxenite	0	94	3	2	< 1	0	< 1	1050–1150	3.0–4.0
18XM7	Porphyroclastic Websterite	0	48	52	0	0	< 1	< 1	1200	3.0

done with an acceleration voltage of 15 kV and a beam current of 5 nA on sample (100 nA for elemental maps). Measurements of all elements have been carried out with a 30 s counting time and with 10 s background-counting time for the positive and negative part each. The natural standards used for the quantification are: omphacite for Na, ilmenite for Ti, rhodonite for Mn, K-feldspar for K, olivine for Mg, grossular for Si, Ca and Al, fayalite 143 for Fe, pure Cr metal for Cr and niccolite for Ni.

3.2. Laser Ablation ICP-MS

The trace elements analyses of all mineral phases have been performed using LA-ICP-MS technology at Institute of Geosciences and Earth Resources of Pavia (C.N.R., Pavia, Italy), using a Perkin Elmer ELAN DRCe quadrupole mass spectrometer coupled with a Q-switched Nd:YAG laser source Brilliant (Quantel, Les Ulis, France). The laser was operated at a repetition rate of 10 Hz, with a pulse energy of ~35 mJ. Helium was used as carrier gas (0.4–0.85 l/min range) and was mixed with Ar downstream of the ablation cell. Spot diameter was adjusted in the range of 40–100 μm. Data reduction was performed offline using the GLITTER software. Precision and accuracy of the trace element concentrations were assessed through repeated analysis of the BCR2-g standard to be better than ±7% and ± 10%, respectively, at the ppm concentration level (Miller et al., 2007 for further details). NIST SRM 610 synthetic glass standard was used as external standard and CaO was used as internal standard for clinopyroxene, SiO2 was used for orthopyroxene and olivine, MgO and Al2O3 were used for spinel, while SiO2 and CaO were used for garnet.

3.3. Electron back scattered diffraction

Electron Back-Scattered Diffraction (EBSD) mapping of full thin-sections of the whole sample suite was performed at the *SEM-EBSD Platform* of Geosciences Montpellier (CNRS & Université de Montpellier, France), using two different instruments: a JEOL 5600 SEM equipped with a Nordlys II EBSD Detector from Oxford Instruments (samples 18XM2, 18XM3, 18XM6, 18XM11, COL1 and COL2) and, for higher resolution analyses, a CamScan X500FE CrystalProbe equipped with a Symmetry CMOS detector from Oxford Instruments (samples 18XM2, 18XM4, 18XM5, 18XM7, 18XM9, and 18XM12). We performed EBSD mapping at 8–30 μm resolution (depending on the grain size, step size being always at least smaller than the minimum grain size) of the entire xenolith sections as well as higher resolution maps of selected areas. The EBSD data was treated using the MTEX open-source toolbox for MATLAB. The output includes phase maps, crystallographic orientation maps (orientation and misorientation distributions), crystallographic preferred orientation (CPO) plots, grains' sizes, shapes and orientations, intracrystalline deformation features, and grain boundary characterization. In the present work, we use the phase maps of all samples to estimate the modal compositions, which are then used to calculate the bulk trace element composition of rock samples (section 8 of this work). We also use the crystallographic orientation maps of samples COL1 and COL2 to gain information on early, pre-deformation, features. The remaining microstructural data will be part of an article focusing on the deformation of these xenoliths, which shortly predated and is associated with the processes leading to their extraction from the mantle wedge (Notini et al., in preparation).

4. Petrography

The majority of Mercaderes mantle xenoliths display porphyroclastic textures, with deformed clinopyroxene, orthopyroxene, garnet and spinel porphyroclasts showing a marked undulose extinction embedded in a fine-grained matrix composed of neoblasts of the same mineral assemblage ± olivine. The different mineral phases show variable responses to deformation: olivine is the weakest phase, followed by ortho and clinopyroxene. In the peridotites (Fig. 2), no olivine porphyroclasts are preserved, coarse olivine is only observed as inclusions in other phases, whereas pyroxene and garnet porphyroclasts have rounded or angular shapes. In orthopyroxenites, orthopyroxene porphyroclasts are very elongated and exhibit well-developed recrystallization tails that, together with the foliated fine-grained matrix, compose a mylonitic texture (Fig. 3). Porphyroclastic garnet-clinopyroxenites and one garnet-free websterite are characterized by irregularly shaped pyroxene and rounded garnet porphyroclasts enclosed in a matrix of pyroxene neoblasts. Garnet appears to be the least deformed mineral in all samples, although in mylonitic samples garnet aggregates may locally occur as flattened thin stripes. Undeformed coarse-grained textures are only preserved in two garnet websterite samples (COL1 and COL2). All xenoliths, except for the spinel lherzolite, contain fine grained aggregates of amphibole (sometimes associated with spinel and orthopyroxene) dispersed within the fine-grained matrix or along grain boundaries between garnet and other phases. The mineral assemblages and mineral modal abundances in all samples are shown in Table 1 and described in

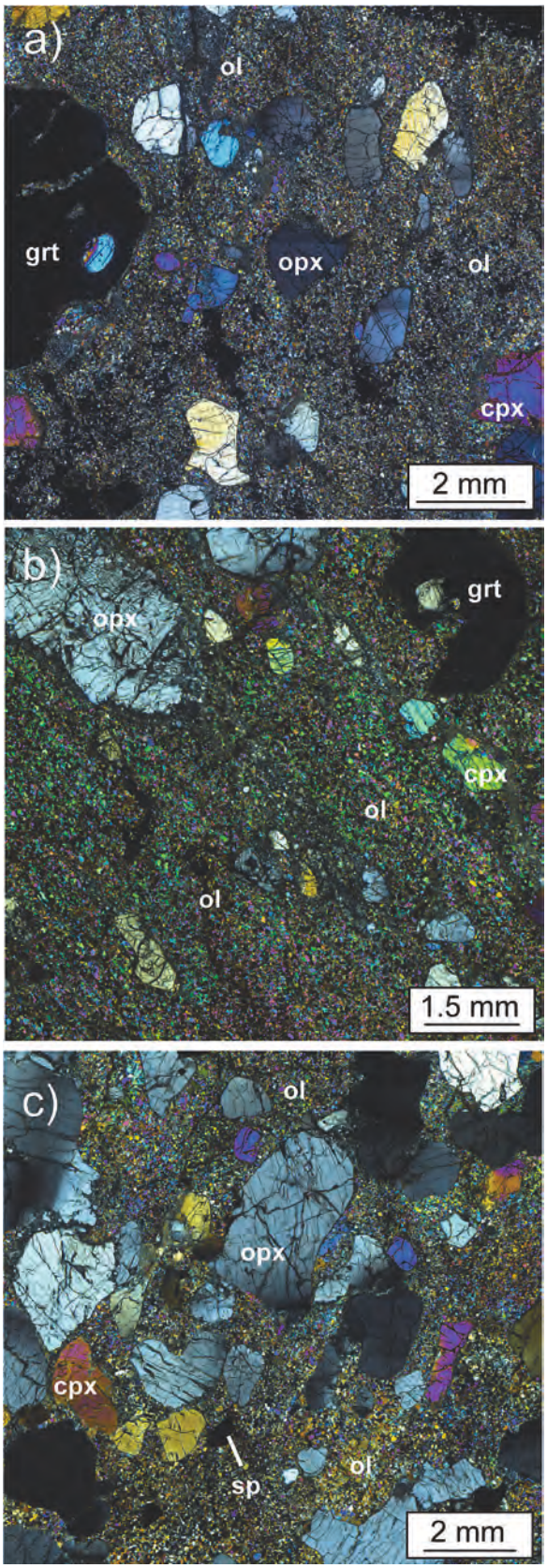

Fig. 2. a) Sample 18XM12 – garnet lherzolite; b) Sample 18XM4 – garnet lherzolite; c) Sample 18XM5 – Spinel lherzolite.

detail in the following sections.

4.1. *Porphyroclastic garnet and spinel lherzolites*

This sample group includes two garnet lherzolites (18XM4; 18XM12; Fig. 2a, b) and one spinel lherzolite (18XM5) of small size (2–4 cm in diameter). The two garnet lherzolite samples contain variable modal amounts of pyroxene (Table 1). Based on the EBSD analysis, 18XM4 shows up to 22% by area of clinopyroxene, whereas 18XM12 has higher modal orthopyroxene and much lower clinopyroxene (11% by area; compare Fig. 2a and b). The spinel lherzolite (Fig. 2c) has an even lower modal content of clinopyroxene (6% by area). All peridotites display clinopyroxene, orthopyroxene ± garnet ± spinel porphyroclasts embedded in a fine-grained matrix composed mainly of olivine with granoblastic texture and homogeneous grain size; porphyroclasts are irregularly shaped with lobes filled by the olivine matrix (Fig. 2a-c). In the garnet lherzolites, very fine-grained aggregates of spinel, amphibole, and orthopyroxene (identified by SEM-WDS analyses) occur at the rims and inside fractures of coarse garnet porphyroclasts. The latter minerals are absent in the spinel lherzolite.

4.2. *Coarse garnet websterites*

Coarse garnet websterites are represented by xenoliths COL1 and COL2 (Fig. 3a, b), which are composed of orthopyroxene, clinopyroxene, and garnet in different modal proportions (Table 1). The variation in modal composition may be due to the coarse grain size (up to 2 cm) compared to the xenolith's dimension (3–4 cm in diameter). Both samples share coarse-granular structures. They are the only samples within the whole Mercaderes mantle xenolith suite that do not show a fine-grained matrix. Both samples are characterized by coarse ortho- and clinopyroxenes with variable size (1 mm - 2 cm) and irregular shapes with interpenetrating contacts. The pyroxene grains do not show any clear elongation but display weak undulous extinction, indicating moderate lattice deformation. Garnet crystals in COL1 and COL2 have different habitus. In COL1 garnet is smaller than pyroxenes, has elongated shapes and dominantly interstitial habitus (Fig. 3a). In COL2 garnet is heterogranular (0.2 to 8 mm), has more idiomorphic shapes and forms aggregates. Amphibole and spinel are accessory minerals, identified through SEM-WDS analysis; they mostly occur at the boundaries between garnet and other phases. Amphibole can be present in appreciable modal amounts (Table 1) as micrometric, interstitial grains. Spinel is rarer and forms smaller crystals always associated with amphibole.

The above observations indicate that xenoliths COL1 and COL2 are only weakly affected by solid-state deformation. The analysis of their microstructure allows therefore constraining the pristine texture of the pyroxenites in the mantle wedge. Fig. 4 shows EBSD-derived crystal orientation maps of clinopyroxene, orthopyroxene, and garnet for the two samples: the colors represent the crystallographic orientation, thus variations in colour shade within a grain correspond to distortions of the crystal lattice generated by deformation, observed optically as undulous extinction. The crystal orientation maps show that clinopyroxene in both samples COL1 and COL2 occurs as coarse anhedral crystals with irregular shapes that share the same crystallographic orientation of nearby finer grains (Fig. 4a and b). This denotes a poikilitic texture. The coarse grains show variations in their colour shade that denote undulose extinction. Coarse orthopyroxene in both samples also displays undulose extinction (Fig. 4c and d). In COL1, garnet displays an interstitial, locally poikilitic texture (Fig. 4e), whereas in sample COL 2, garnet forms elongated aggregates of irregularly shaped crystals, but the crystal lattices are not distorted, indicating that the grains are not deformed (Fig. 4f).

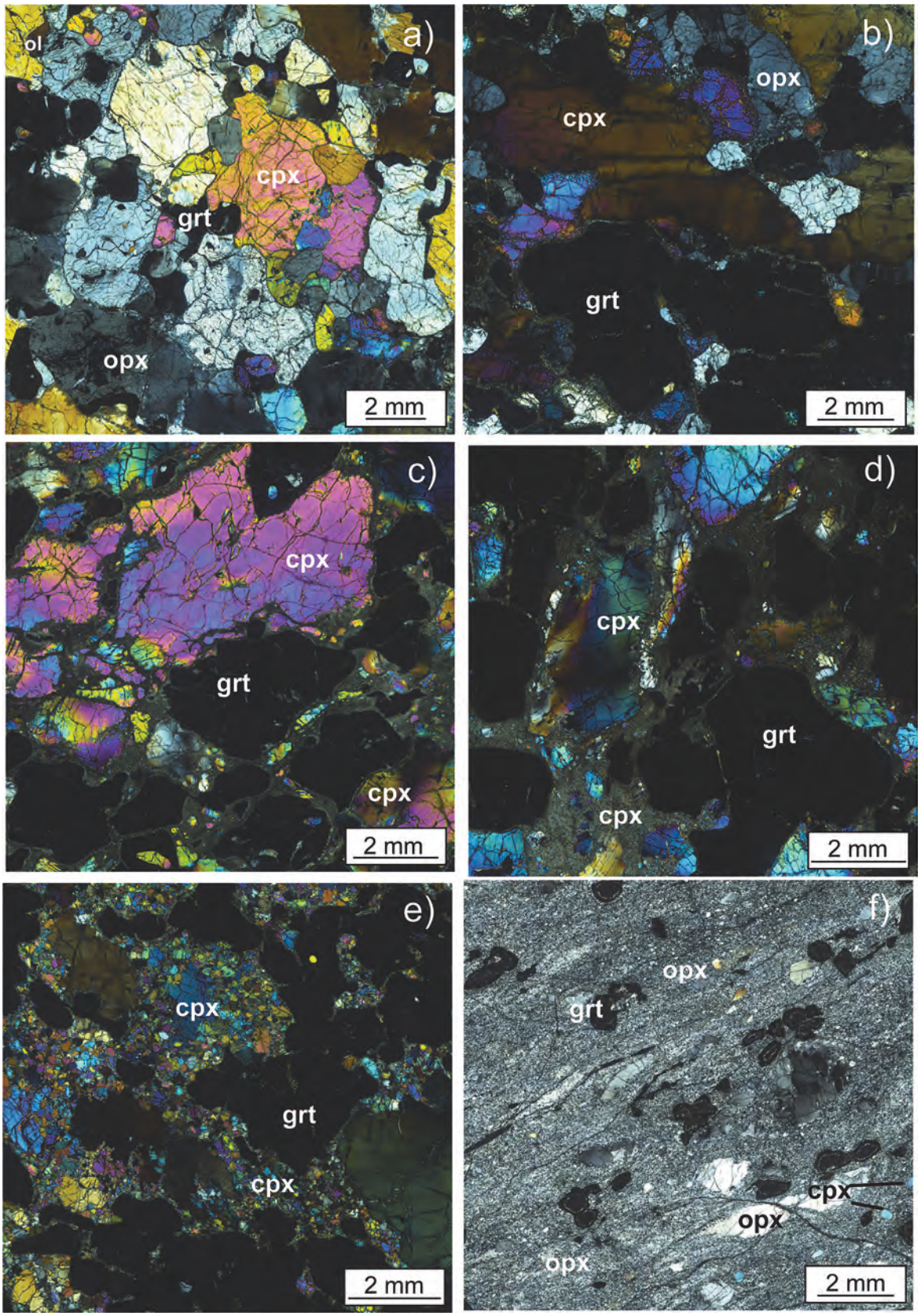

Fig. 3. a) Sample COL1 – garnet websterite; b) Sample COL2 – garnet websterite; c) Sample 18XM6 – garnet clinopyroxenites; d) 1Sample 18XM11 – garnet clinopyroxenites; e) Sample 18XM9 – garnet clinopyroxenites; f) Sample 18XM3 – mylonitic orthopyroxenite.

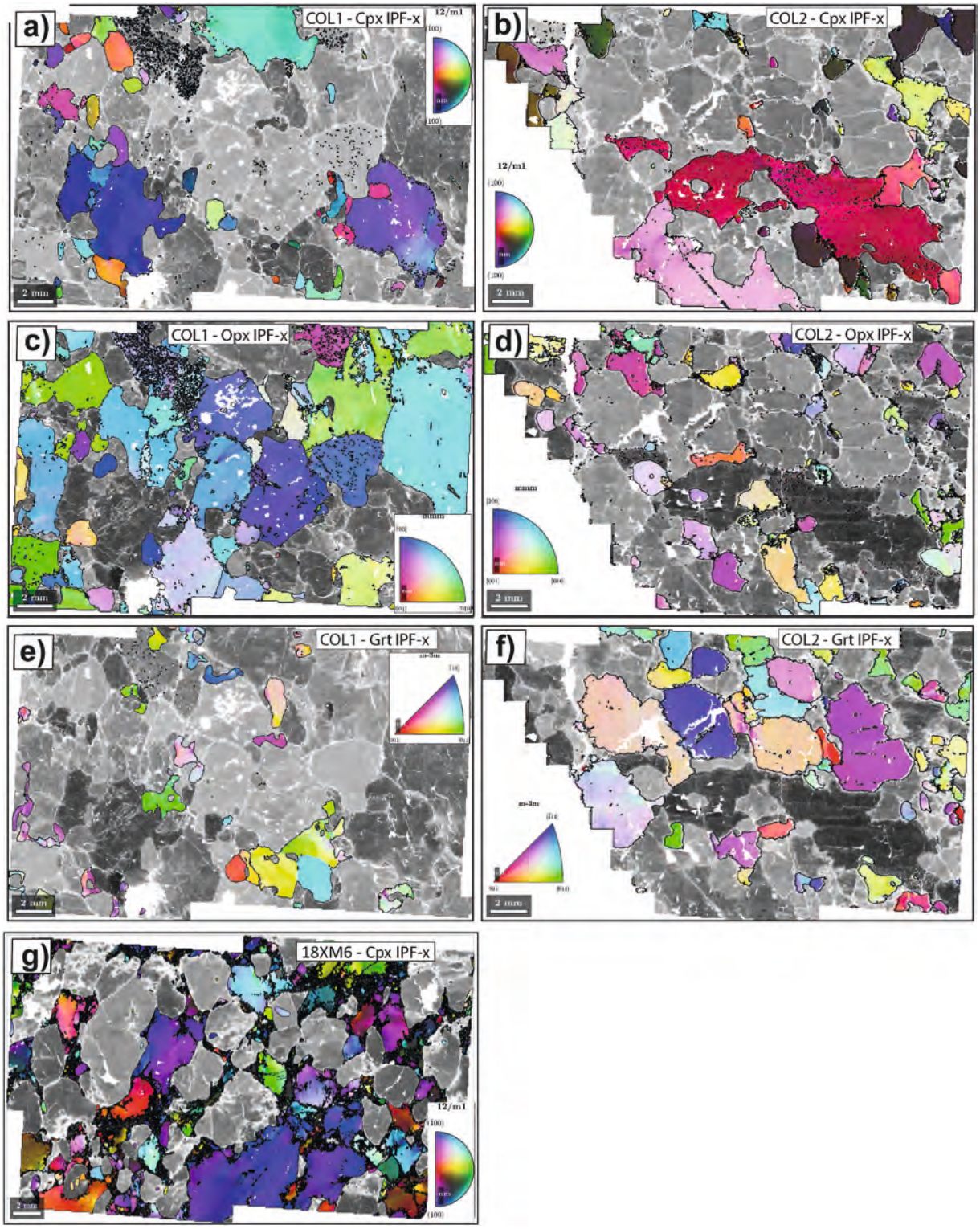

Fig. 4. EBSD IPF (Inverse Pole Figure) for samples COL1 and COL2. Every colour is associated to a particular crystallographic orientation, with proportionality between colour differences and orientation differences. a) Sample COL1 – clinopyroxene IPF; b) Sample COL2 – clinopyroxene IPF; c) Sample COL1 – orthopyroxene IPF; d) Sample COL2 – orthopyroxene IPF; e) Sample COL1 – garnet IPF; f) Sample COL2 – garnet IPF; g) EBSD-derived crystal-orientation map of clinopyroxene, sample 18XM6. Colour shades indicate the orientation of the thin section long axis relative to the local crystal reference frame of clinopyroxene, so a grain is defined as a contiguous domain with similar colors. The tone variations within a grain indicate distortion of the crystal lattice due to the accumulation of dislocations, optically observed as undulose extinction. Garnet is displayed in gray levels, as a function of the quality of the diffraction patterns. White areas are non-diffracting domains: fractures, alteration, and fragments scraped off during thin section preparation.

4.3. Porphyroclastic garnet clinopyroxenites

Xenoliths 18XM6, 18XM9, and 18XM11 (Figs. 3c, d, e), which are 3 to 5 cm wide, consist of coarse garnet and clinopyroxene porphyroclasts enclosed in a fine-grained clinopyroxene matrix (Table 1). The three samples differ by the average grain size of the matrix, which varies from 53 μm in 18XM6 to 115 μm in 18XM11, and 207 μm in 18XM9. They also differ by the volume fraction of the matrix, which is the lowest (<20%) in 18XM6. In all garnet clinopyroxenites, the clinopyroxene porphyroclasts have marked undulous extinction and kink bands and display irregular shapes with sinuous grain boundaries with embayments filled by a clinopyroxene-rich matrix. The clinopyroxene porphyroclasts are frequently cut by micro-cracks rimmed by recrystallized grains, which do not extend into the matrix. Garnet porphyroclasts (0.3 mm to 1 cm in size) have irregular, but rounded shapes. Garnet porphyroclasts may occur as elongated lenses marking a rough layering, especially in sample 18XM11. Accessory very fine-grained amphibole, orthopyroxene, and subordinated spinel are observed at the rims and in fractures within garnet porphyroclasts and as interstitial phases in the matrix. Amphibole is the most frequent accessory phase, followed by orthopyroxene (Table 1).

The garnet clinopyroxenite 18XM6 is the sample in this group the least reworked by the late high-stress deformation. The EBSD-derived crystal orientation maps of this sample may thus help to unravel its microstructure prior to this deformation. The lack of grain elongation of both clinopyroxene and garnet and the limited recrystallization of clinopyroxene indicate that finite strain during the high-stress event remained small, essentially producing undulose extinction in the clinopyroxenes (Fig. 4g). These data imply that this garnet clinopyroxenite had an initially coarse-granular microstructure, composed of millimetric garnet and clinopyroxene grains. Garnet has irregular but rounded shapes, whereas clinopyroxene has more interstitial shapes (Fig. 4g).

4.4. Porphyroclastic garnet orthopyroxenites

Xenoliths 18XM2 and 18XM3 (2.5 cm to 5 cm in size) are mainly composed of orthopyroxene (88–94%) with subordinated garnet and clinopyroxene (Table 1; Fig. 3f). Both samples display orthopyroxene, garnet, and clinopyroxene porphyroclasts embedded in a very fine-grained orthopyroxene-rich matrix. The matrix/porphyroclast ratio varies between the two samples: 18XM2 mostly consists of orthopyroxene porphyroclasts with scarce interstitial fine-grained matrix (matrix/porphyroclasts area ratio = ~20/80), whereas in 18XM3 the fine-grained matrix predominates (matrix/porphyroclasts area ratio = 85/15). The orthopyroxene porphyroclasts have heterogenous grain size (0.5 mm - 6 mm). They may be extremely elongated (aspect ratios up to 10:1), and display kink bands, undulous extinction and micro-cracks. In 18XM3, the larger orthopyroxene porphyroclasts display tension cracks (normal to the grain elongation) filled with micro-crystalline clinopyroxene. Garnet and clinopyroxene porphyroclasts in both samples are smaller than orthopyroxene ones (grain size between 0.1 mm and 3 mm). Clinopyroxene porphyroclasts usually display recrystallization tails. In 18XM3, intergrows of amphibole, spinel, and orthopyroxene rimming garnet porphyroclasts were observed through both EBSD and SEM-WDS analysis and imagery.

4.5. Garnet-free websterite

Xenolith 18XM7 (4 cm in size) consists of clino- and orthopyroxene porphyroclasts in a matrix composed of sub-millimetric clinopyroxene-rich domains around the clinopyroxene porphyroclasts and fine-grained orthopyroxene-rich domains around the orthopyroxene porphyroclasts. Both pyroxene porphyroclasts have slightly irregular grain boundaries, variable grain size (0.2 to 6 mm), and display weak undulous extinction. Unlike the other xenoliths in this suite, no accessory mineral phases have been found in this sample.

5. Mineral compositions

5.1. Major elements

SEM-WDS point analyses have been performed on porphyroclastic and matrix olivine, clinopyroxene, orthopyroxene, garnet, and spinel from all samples together with core to rim profiles and elemental maps of selected porphyroclasts to test possible compositional zoning. Representative major element analyses are shown in Table 2 (the entire major element dataset is reported in the Repository Table R1); the Fe_2O_3 and Fe^{3+} contents of pyroxenes and garnet reported in Table 2b and the garnet andradite end-member contents reported in Fig. 5 have been computed using the methods of Droop (1987) and Locock (2008), respectively. The variability in the major element composition of rock forming minerals from all samples is shown in Fig. 5. In all samples, minerals display homogeneous composition and a lack of zoning; this is shown in Fig. 6 that portrays, as an example, data for the garnet-websterite and garnet-orthopyroxenite samples.

5.2. Porphyroclastic garnet and spinel lherzolites

The rock-forming minerals of garnet- and spinel-lherzolites (18XM4, 18XM12, 18XM5) display homogeneous core-to-rim compositions. Clinopyroxene is diopside with Mg# between 88 and 91 and low Na content (Fig. 5a). In garnet lherzolites the Al content of clinopyroxene is lower than in the spinel lherzolite (Fig. 5b). Clinopyroxene in spinel lherzolite has also higher Cr than clinopyroxene in the garnet lherzolites (Fig. 5c). In all samples, Ti in clinopyroxene is relatively low (Fig. 5d). Orthopyroxene has Mg# comprised between 90 and 91.5 in all lherzolites. In garnet lherzolites the orthopyroxene content is lower than in the spinel lherzolite (Fig. 5e). Olivine has homogenous compositions across all lherzolites, with Mg# ranging 90–90.5 (Table 2b). The amount of Fe^{3+} in the above minerals ranges from 0 apfu in olivine and from 0.00 to 0.04 apfu in pyroxene. Garnet has also homogenous compositions, consisting of 75% pyrope and a 50/50 ratio of grossular + andradite and almandine + spessartine components (see Fig. 5f); the amount of andradite end-member ranges from 0.12 to 1.46 mol%.

5.3. Coarse garnet websterites

Samples COL1 and COL2 contain minerals with comparable composition. Clinopyroxene corresponds to diopside with constant Mg# 89. In COL1 Clinopyroxene has higher Na and Al contents than in COL2 (Fig. 5a, b), while in COL2 the clinopyroxene has slightly higher Cr contents (Fig. 5c). The Ti abundance in clinopyroxene is comparable in both samples (Fig. 5d). Orthopyroxene has Mg# 89.5–91 and its Al content is slightly lower in COL2 (Fig. 5e). Clino- and orthopyroxene from these pyroxenite samples have low Fe3+, ranging from 0.00 to maximum 0.04 apfu. In both samples garnet contains around 75% pyrope, with a 50/50 ratio between grossular + andradite and almandine + spessartine endmembers (Fig. 5f), and 1 to 1.54 mol% andradite. Porphyroclastic and matrix minerals have similar compositions, as highlighted by the flat WDS profiles obtained across contiguous grains in COL1(Fig. 6a).

5.4. Porphyroclastic garnet clinopyroxenites

Major rock-forming minerals in the garnet clinopyroxenites display homogeneous compositions within a single sample, but large chemical heterogeneity between different samples (Fig. 5). Clinopyroxene in sample 18XM11 exhibits lower Na, Cr and higher Al contents, and the lowest Mg# values (82–84). Clinopyroxene in sample 18XM6 shows higher Cr and lower Ti and Al abundances coupled to the highest Mg# values (90–91). The Fe3+ content in the clinopyroxenes is low, between 0.00 and 0.04 apfu. Garnet compositions also vary among samples, being around 77% pyrope in 18XM6, 75% pyrope in 18XM9, and 63%

Table 2
a, b. Representative analyses of rock-forming minerals from selected samples of the Mercaderes Xenolith suite with major elements (wt%) and cation proportions (apfu).

	Grt peridotite												**Grt webst**									
	18XM4 30-A1-7 Ol m	18XM4 30-A3-7 Ol m	18XM4 30A1-1 Cpx c	18XM4 30-A1-2 Cpx r	18XM4 30-A1-9 Cpx m	18XM4 30-A4-3 Opx c	18XM4-30-A4 4 Opx r	18XM4-30-A4-5 Opx m	18XM430 -A3-8 Grt c	18XM4 30-A3-9 Grt r	18XM4 30-A5-P20 Grt c	18XM4 30-A5-P18 Grt r	COL1 A2-1 Cpx c	COL1-A2-2 Cpx r	COL2 A1-4 cpx c	COL1 A1-8 Opx c	COL1 A1-7 Opx r	COL2 A1-7 Opx c	COL1 A2-6 Grt c	COL1 A2-5 Grt r	COL2 A1-1 Grt c	COL2 A1-2 rim
SiO_2	41.08	40.65	54.37	54.13	54.44	56.62	56.07	56.93	43.14	42.79	43.18	42.72	53.65	53.73	53.63	55.91	56.00	56.02	42.72	42.88	42.72	42.24
TiO_2	0.03	0.00	0.41	0.42	0.24	0.22	0.13	0.13	0.33	0.30	0.33	0.36	0.31	0.29	0.31	0.12	0.10	0.15	0.33	0.24	0.26	0.24
Al_2O_3	0.03	0.04	4.05	3.89	1.57	2.19	2.12	1.79	22.89	23.03	22.53	22.43	5.57	5.48	4.52	3.95	3.81	3.00	23.52	23.59	23.44	22.89
Cr_2O_3	0.02	0.02	1.02	1.02	1.24	0.40	0.32	0.37	1.65	1.37	1.43	1.72	0.41	0.51	0.66	0.32	0.37	0.31	0.63	0.66	1.06	1.07
FeO	9.84	9.85	2.72	2.39	2.96	6.09	5.00	5.78	7.72	7.22	7.04	7.27	2.96	2.52	3.23	5.8	6.37	5.42	6.47	6.87	7.31	6.75
Fe_2O_3calc	0.00	0.00	1.16	1.65	0.84	0.00	1.22	0.31	0.00	0.33	0.78	0.56	0.97	1.45	0.48	0.48	0.00	1.10	0.82	0.41	0.27	0.65
MnO	0.12	0.11	0.17	0.09	0.10	0.10	0.09	0.11	0.29	0.23	0.32	0.34	0.08	0.12	0.08	0.12	0.10	0.14	0.31	0.21	0.24	0.27
MgO	49.38	49.49	17.17	17.08	17.43	33.25	33.49	33.33	20.89	21.02	21.48	21.35	17.45	17.64	17.44	32.50	32.47	32.36	21.65	21.53	20.93	20.93
NiO	0.42	0.37	0.04	0.00	0.01	0.11	0.16	0.11	0.05	0.00	0.04	0.048	0.11	0.06	0.00	0.11	0.09	0.10	0.00	0.02	0.00	0.05
CaO	0.10	0.07	17.63	17.73	20.84	1.07	1.07	1.13	4.79	4.90	4.60	4.68	16.62	16.81	17.91	1.30	1.30	1.26	4.58	4.60	4.82	4.95
Na_2O	0.02	0.01	2.00	2.04	0.96	0.19	0.21	0.31	0.00	0.05	0.06	0.06	1.94	1.91	1.51	0.31	0.27	0.19	0.03	0.03	0.06	0.01
K_2O	0.00	0.01	0.01	0.00	0.01	0.00	0.01	0.00	0.01	0.01	0.00	0.00	0.00	0.01	0.02	0.00	0.00	0.01	0.00	0.00	0.00	0.00
Total	101.03	100.62	100.75	100.44	100.54	100.24	99.89	100.30	101.76	101.21	101.7243	101.93	100.07	100.53	99.79	100.89	100.88	99.95	100.97	100.98	101.08	100.00
Si	1.00	0.99	1.94	1.94	1.97	1.95	1.94	1.96	3.01	2.99	3.01	3.01	1.93	1.92	1.93	1.92	1.92	1.94	2.98	2.99	2.99	2.99
Ti	0.00	0.00	0.01	0.01	0.01	0.01	0.00	0.00	0.02	0.02	0.02	0.02	0.01	0.01	0.01	0.00	0.00	0.00	0.02	0.01	0.01	0.01
Al	0.00	0.00	0.17	0.16	0.07	0.09	0.09	0.07	1.88	1.90	1.85	1.84	0.24	0.23	0.20	0.16	0.15	0.12	1.94	1.94	1.93	1.91
Cr	0.00	0.00	0.03	0.03	0.04	0.01	0.01	0.01	0.09	0.08	0.08	0.09	0.01	0.01	0.02	0.01	0.01	0.01	0.04	0.04	0.06	0.06
Fe^{2+}	0.20	0.20	0.08	0.07	0.09	0.10	0.14	0.17	0.45	0.42	0.41	0.41	0.09	0.07	0.10	0.17	0.18	0.16	0.38	0.40	0.43	0.40
Fe^{3+}	0.00	0.00	0.03	0.04	0.02	0.00	0.03	0.01	0.00	0.02	0.04	0.03	0.03	0.04	0.01	0.01	0.00	0.03	0.04	0.04	0.01	0.03
Mn	0.00	0.00	0.01	0.00	0.00	0.00	0.00	0.00	0.02	0.01	0.02	0.02	0.00	0.00	0.00	0.00	0.00	0.00	0.02	0.01	0.01	0.02
Mg	1.79	1.80	0.92	0.92	0.94	1.71	1.73	1.71	2.17	2.19	2.23	2.22	0.93	0.94	0.94	1.66	1.66	1.67	2.25	2.24	2.18	2.21
Ni	0.01	0.01	0.00	0.00	0.00	0.00	0.00	0.00	0.00	0.00	0.00	0.00	0.00	0.00	0.00	0.00	0.00	0.00	0.00	0.00	0.00	0.00
Ca	0.00	0.00	0.68	0.68	0.81	0.04	0.04	0.04	0.36	0.37	0.34	0.35	0.64	0.64	0.68	0.05	0.05	0.05	0.34	0.34	0.36	0.38
Na	0.00	0.00	0.14	0.14	0.07	0.01	0.01	0.02	0.00	0.01	0.01	0.01	0.14	0.13	0.11	0.02	0.02	0.01	0.00	0.00	0.01	0.00
K	0.00	0.00	0.00	0.00	0.00	0.00	0.00	0.00	0.00	0.00	0.00	0.00	0.00	0.00	0.00	0.00	0.00	0.00	0.00	0.00	0.00	0.00
Total	3.00	3.01	4.01	4.01	4.01	4.00	4.01	4.00	7.99	8.01	8.01	8.01	4.01	4.01	4.01	4.01	4.00	4.00	8.01	8.01	8.00	8.01
XMg	0.90	0.90	0.89	0.89	0.89	0.91	0.91	0.91	0.83	0.83	0.83	0.83	0.89	0.89	0.90	0.90	0.90	0.90	0.84	0.84	0.83	0.84

(*continued on next page*)

Table 2 (*continued*)

	Grt clinopiroxenite								Grt orthopyroxenite								Websterite					
	18XM6 30-A2-4 Cpx c	18XM6 30A2-7 Cpx r	18XM6 30-A2-10 Cpx m	18XM11 30-A1-9 Cpx c	18XM6 30-A1-13 Opx m	18XM6 30-A2-1 Grt c	18XM6 30-A2-2 Grt r	18XM11 30-A1-15 Grt c	18XM2 A1-1 Cpx c	18XM2 A1-2 Cpx r	18XM2 A1-3 Cpx m	18XM2 A2-7 Opx c	18XM2 A2-8 Opx r	18XM2 A2-11 Opx m	18XM2 A2-10 Grt c	18XM2 A2-9 Grt r	18XM7 30-A1-1 Cpx c	18XM7 30-A1-2 Cpx r	18XM7 30-A1-5 Cpx m	18XM7 30-A1-9 Opx c	18XM7 30-A1-10 Opx r	18XM7 30-A1-15 Opx m
SiO_2	55.33	55.00	55.00	51.75	56.55	43.29	43.03	42.21	54.58	53.76	54.53	56.97	57.47	56.75	42.51	42.68	53.85	54.00	54.11	56.76	55.90	55.67
TiO_2	0.28	0.22	0.22	0.27	0.10	0.27	0.21	0.14	0.08	0.19	0.08	0.06	0.07	0.00	0.15	0.21	0.08	0.12	0.14	0.03	0.08	0.13
Al_2O_3	3.26	3.14	3.11	5.28	2.47	23.51	23.22	23.19	3.15	3.23	2.90	2.01	2.15	2.31	21.29	21.42	3.09	3.19	3.09	2.88	2.97	3.31
Cr_2O_3	0.57	0.59	0.65	0.07	0.42	0.72	0.94	0.11	1.48	1.37	1.49	0.58	0.59	0.53	3.19	3.16	0.73	0.68	0.83	0.67	0.52	0.54
FeO	3.09	2.30	3.29	4.73	7.11	7.36	6.86	11.05	2.84	2.04	3.17	6.07	5.85	5.73	6.48	6.61	4.18	4.31	4.12	7.97	7.77	7.18
Fe_2O_3calc	0.14	1.19	0.23	1.31	0.00	0.00	0.80	0.92	0.47	1.41	0.00	0.00	0.00	0.02	0.95	0.85	0.00	0.00	0.00	0.00	0.12	1.05
MnO	0.09	0.07	0.09	0.15	0.12	0.29	0.25	0.42	0.10	0.09	0.07	0.13	0.11	0.10	0.27	0.21	0.07	0.04	0.14	0.22	0.18	0.17
MgO	17.48	17.78	17.51	15.66	33.17	21.45	21.58	17.55	17.49	17.61	17.47	33.27	33.41	33.26	20.81	20.94	17.45	17.66	17.58	32.08	32.09	32.27
NiO	0.07	0.00	0.05	0.00	0.10	0.02	0.00	0.01	0.09	0.01	0.07	0.12	0.15	0.10	0.00	0.00	0.00	0.06	0.08	0.08	0.17	0.08
CaO	18.62	18.71	18.54	20.08	0.72	4.59	4.62	6.12	18.74	18.64	18.59	1.08	1.11	1.21	5.38	5.37	20.13	20.18	20.39	1.24	1.10	1.08
Na_2O	1.76	1.71	1.63	0.77	0.06	0.01	0.03	0.00	1.77	1.52	1.52	0.23	0.14	0.25	0.02	0.07	0.56	0.61	0.55	0.04	0.06	0.06
K_2O	0.02	0.00	0.02	0.01	0.00	0.00	0.00	0.00	0.00	0.00	0.00	0.01	0.01	0.02	0.00	0.00	0.00	0.00	0.00	0.00	0.00	0.01
Total	100.71	100.72	100.34	100.08	100.82	101.50	101.46	101.63	100.78	99.86	99.88	100.53	101.06	100.28	100.99	101.40	100.13	100.85	101.04	101.97	100.96	101.54
Si	1.98	1.97	1.97	1.89	1.94	3.01	3.00	3.00	1.95	1.95	1.97	1.96	1.96	1.95	3.00	3.00	1.95	1.94	1.94	1.94	1.93	1.92
Ti	0.01	0.01	0.01	0.01	0.00	0.01	0.01	0.01	0.02	0.01	0.00	0.00	0.00	0.00	0.01	0.01	0.00	0.00	0.00	0.00	0.00	0.00
Al	0.14	0.13	0.13	0.23	0.10	1.93	1.91	1.94	0.13	0.14	0.12	0.08	0.09	0.09	1.77	1.78	0.13	0.14	0.13	0.12	0.12	0.13
Cr	0.02	0.02	0.02	0.00	0.01	0.04	0.05	0.01	0.04	0.04	0.04	0.02	0.02	0.01	0.18	0.18	0.02	0.02	0.02	0.02	0.01	0.01
Fe^{2+}	0.09	0.07	0.10	0.14	0.21	0.43	0.40	0.66	0.08	0.06	0.10	0.17	0.17	0.17	0.39	0.38	0.13	0.13	0.12	0.23	0.23	0.21
Fe^{3+}	0.00	0.03	0.01	0.04	0.00	0.00	0.04	0.05	0.01	0.04	0.00	0.00	0.00	0.00	0.04	0.05	0.00	0.00	0.00	0.00	0.01	0.03
Mn	0.00	0.00	0.00	0.00	0.00	0.02	0.01	0.03	0.00	0.00	0.00	0.00	0.00	0.00	0.02	0.01	0.00	0.00	0.00	0.01	0.01	0.00
Mg	0.93	0.95	0.94	0.85	1.70	2.22	2.24	1.86	0.93	0.95	0.94	1.70	1.70	1.71	2.19	2.20	0.94	0.95	0.94	1.63	1.65	1.66
Ni	0.00	0.00	0.00	0.00	0.00	0.00	0.00	0.00	0.00	0.00	0.00	0.00	0.00	0.00	0.00	0.00	0.00	0.00	0.00	0.00	0.00	0.00
Ca	0.71	0.72	0.71	0.79	0.03	0.34	0.34	0.47	0.71	0.72	0.72	0.04	0.04	0.04	0.41	0.40	0.78	0.78	0.78	0.05	0.04	0.04
Na	0.12	0.12	0.11	0.05	0.00	0.00	0.00	0.00	0.12	0.11	0.11	0.02	0.01	0.02	0.00	0.01	0.04	0.04	0.04	0.00	0.00	0.00
K	0.00	0.00	0.00	0.00	0.00	0.00	0.00	0.00	0.00	0.00	0.00	0.00	0.00	0.00	0.00	0.00	0.00	0.00	0.00	0.00	0.00	0.00
Total	4.00	4.01	4.00	4.01	4.00	8.00	8.01	8.02	4.00	4.01	4.00	4.00	3.99	4.00	8.01	8.02	3.99	4.00	4.00	3.99	4.00	4.01
XMg	0.91	0.90	0.90	0.83	0.89	0.84	0.84	0.72	0.91	0.90	0.91	0.91	0.91	0.91	0.83	0.84	0.88	0.88	0.88	0.88	0.88	0.88

pyrope in 18XM11. In all three samples garnet has a 50/50 ratio of grossular + andradite and almandine + spessartine components (Fig. 5f), with 2 and 2.3 mol% of andradite, and a higher Fe^{3+} content than the other lithologies.

5.5. Porphyroclastic garnet orthopyroxenites

Orthopyroxenites (18XM2 and 18XM3) have homogenous mineral compositions within a sample. No chemical zoning is observed between cores and rims of porphyroclasts. Moreover, porphyroclasts and the fine-grained matrix have similar compositions (Fig. 6b). Clinopyroxene, which occurs in very low modal abundance (<3% volume), is diopside with Mg# of 90–92 (higher values for 18XM3 – Fig. 4a). Na and Al contents in clinopyroxene are slightly higher in 18XM2 than 18XM3 (Figs. 5a, b). The Cr content in clinopyroxene is high (Fig. 5c) and the Ti content in clinopyroxene is low in the two samples (Fig. 5d) with Fe^{3+} content of 0.04 apfu. Orthopyroxene has Mg# of 90.5–92.5, low Al (Fig. 5e) and no Fe^{3+} contents. Garnet compositions are similar to those of garnet from most other samples in the suite, around 75% pyrope and a 50/50 ratio between grossular + andradite and Almandine + spessartine components (Fig. 5f). In garnet orthopyroxenites, the garnet has from 1 to 2.6 mol% of andradite, a bit higher than in the other lithologies.

5.6. Garnet-free websterite

The only websterite sample (18XM7) also displays homogenous mineral compositions in cores and rims of porphyroclasts and in the recrystallized matrix. Clinopyroxene has Mg# of 88–89, low Na and Ti, and variable Al contents (Fig. 5). Orthopyroxene is enstatite with Mg# between 87 and 88.5, with a moderate Na content (Fig. 5e).

5.7. Trace elements

LA-ICP-MS analyses have been performed on core and rims of rock-forming minerals from all samples. REE and trace element mineral analyses are reported in Table 3a, b and in Fig. 7, where all trace element values are normalized to primitive mantle (PM - McDonough and Sun, 1995). The full dataset of major element mineral compositions is reported in the supplementary Table 2 s. The REE spectra and spider diagrams are quite heterogeneous among the different lithologies, but except for garnet clinopyroxenites, different samples from a given lithology display similar patterns. Trace element compositions of core and rim domains of the same mineral are homogeneous.

5.8. Porphyroclastic garnet and spinel lherzolites

The PM-normalized REE compositions of minerals from garnet and spinel lherzolites are shown in Fig. 7a. In the spinel lherzolite 18XM5, clinopyroxene is compositionally homogeneous and characterized by LREE depletion (La—Ce abundances slightly below the PM value) and flat M-HREE patterns. The coexisting orthopyroxene shows LREE depletion (La_N/Sm_N = 0,38) and HREE concentrations around the PM.

In the garnet lherzolites, clinopyroxene displays LREE depletion, a flat MREE pattern, and a slight depletion in HREE (Dy_N/Yb_N = 4.54). The absolute REE contents are higher in sample 18XM4 compared to 18XM12. Garnet shows significant LREE depletion (La_N/Sm_N = 0.01) and flat to fractionated HREE profiles (Dy_N/Yb_N = 1.17). Orthopyroxene from garnet lherzolites has lower REE contents compared to the spinel lherzolite. Spider diagrams for spinel and garnet lherzolite are shown in Fig. 7b; Pb and Li show a negative anomaly in clinopyroxene and garnet and a positive anomaly in orthopyroxene and olivine.

5.9. Coarse garnet websterites

The REE compositions of minerals from garnet websterites are shown in Fig. 7c. In the two samples, garnet and pyroxenes have quite similar REE profiles. Clinopyroxene is depleted in HREE (Dy_N/Yb_N = 2.57) and enriched in LREE (La_N/Sm_N = 0.66). The REE composition of garnet is complementary to clinopyroxene, being characterized by LREE depletion (La_N/Sm_N around 0.2) and flat HREE profile. Orthopyroxene has relatively flat profiles with absolute contents around 0.1 PM and a slight depletion in LREE (La_N/Sm_N ratio around 0.3).

Spider diagrams for garnet websterites are shown in Fig. 7d; Pb and Li show a negative anomaly in clinopyroxene and garnet and a positive anomaly in orthopyroxene and olivine. Sr in garnet and orthopyroxene show a negative anomaly.

5.10. Porphyroclastic garnet clinopyroxenites

The REE compositions of minerals from garnet clinopyroxenites are shown in Fig. 7e. clinopyroxene and garnet in the three samples define similar chemical heterogeneity as observed for the major elements.

Clinopyroxene is variably depleted in LREE in the different samples, all having La_N/Sm_N ratio below 1 (18XM6 = 0.5; 18XM9 = 0.4; 18XM11 = 0.2). They also show HREE depletion with Dy_N/Yb_N (18XM6 = 8; 18XM9 = 5; 18XM11 = 1,5). Clinopyroxene from sample 18XM11 has the highest HREE and lowest LREE contents if compared to the companion samples from this category. Clinopyroxene from sample 18XM6 has lower trace elements abundances than 18XM9, especially in the HREE range, whereas clinopyroxene from sample 18XM9 exhibit the highest LREE concentrations.

The REE patterns of garnet from all clinopyroxenite samples are strongly depleted in LREE (La_N/Sm_N ratio between 0.01 and 0.01 for all samples). Samples 18XM6 and 18XM9 show flat HREE profiles, whereas 18XM11 shows HREE enrichment up to 20–30 times primordial mantle and fractionation Dy_N/Yb_N = 0.49.

Spider diagrams for garnet clinopyroxenites are shown in Fig. 7f. Pb shows a negative anomaly in clinopyroxene and a positive anomaly in garnet. Sr and Li show a negative anomaly in garnet and a positive anomaly in clinopyroxene.

5.11. Porphyroclastic garnet orthopyroxenites

REE mineral compositions for orthopyroxenites 18XM2 and 18XM3 are shown in Fig. 7g. Minerals in these samples have the lowest REE abundances in the entire xenolith suite. Clinopyroxene shows slight LREE depletion (La_N/Sm_N = 0.7–0.9) and very low HREE contents. Garnet exhibits LREE depletion (La_N/Sm_N = 0.06–0.2) and HREE absolute concentrations around 1× PM. Orthopyroxene holds a very low amount of REE; it displays fragmented REE profiles with most elements under the detection limit. Spider diagrams for orthopyroxenites are shown in Fig. 7h; Sr and Li show a negative anomaly in garnet and a positive anomaly in clinopyroxene.

5.12. Garnet-free websterite

REE mineral compositions for websterite 18XM7 are shown in Fig. 7i. Clinopyroxene shows LREE depletion (La_N/Sm_N = 0.2–0.3) and flat HREE spectra at about 1× PM. The orthopyroxene LREE composition is mostly under detection limit, whereas HREE show a moderate enrichment defined by the slight positive slope of the profile. Spider diagrams for websterites are shown in Fig. 7j. Clinopyroxene shows a positive anomaly in Pb and a negative one in Zr, whereas orthopyroxene shows a positive anomaly in Li.

6. Geothermobarometry

The pressure-temperature (*P-T*) equilibration conditions of xenoliths have been obtained by applying several geothermometric and geobarometric calibrations to core-core pairs and adjacent rim domains of garnet, clino and orthopyroxene porphyroclasts and grains from the fine-grained matrix. For temperature estimates we used the Nimis and

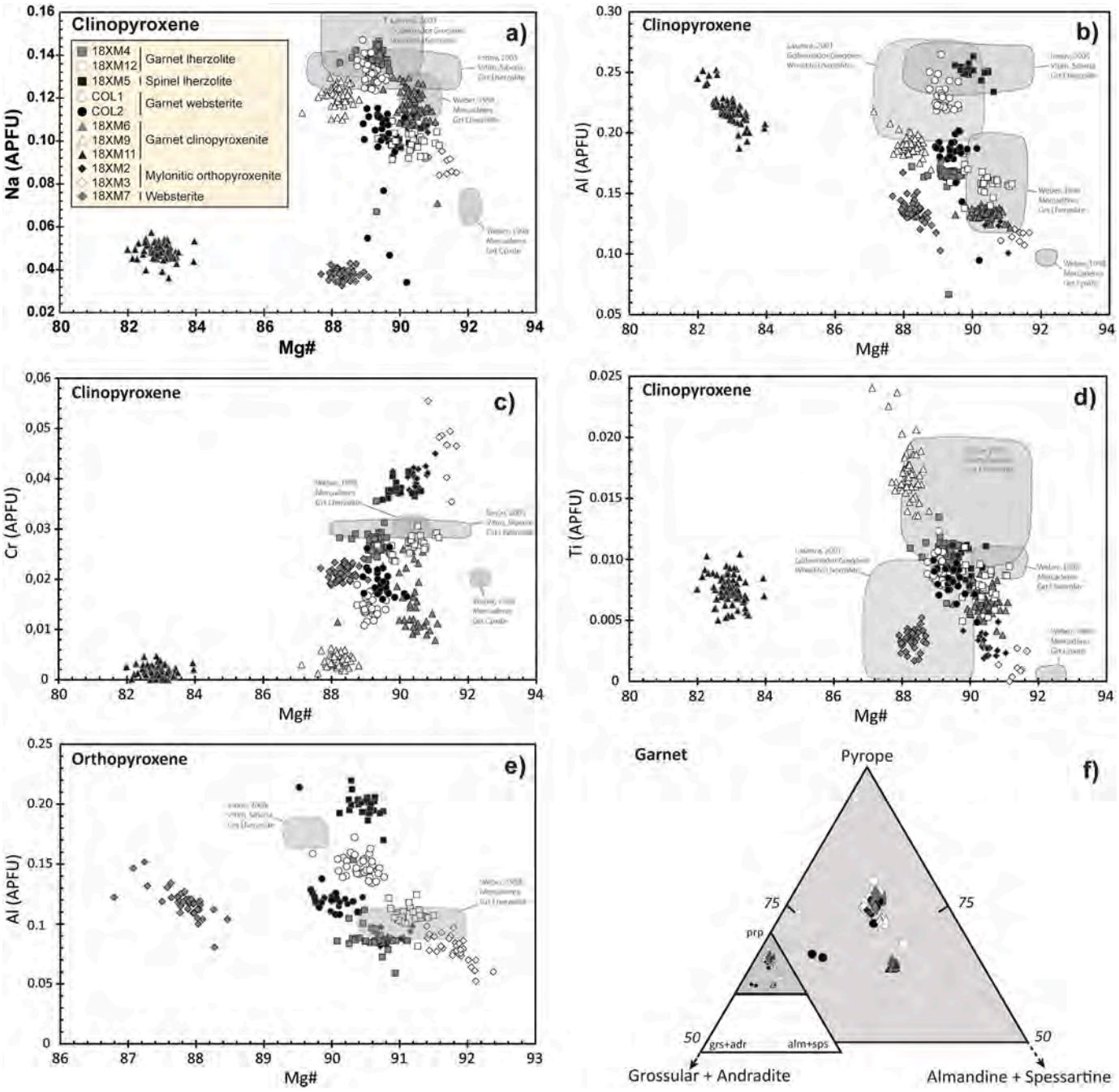

Fig. 5. Major element mineral compositions obtained through SEM-WDS analysis: a) Clinopyroxene Na vs Mg#; b) Clinopyroxene Al vs Mg#; c) Clinopyroxene Cr vs Mg#; d) Clinopyroxene Ti vs Mg#; e) Orthopyroxene Al vs Mg#; f) Garnet compositional triangle plot.

Taylor (2000), Taylor (1998), Brey and Köhler (1990), and Harley (1984) calibrations. For pressure estimates we adopted the Nimis and Taylor (2000), Nickel and Green (1985), Brey and Köhler (1990) and Brey et al. (2008) calibrations. For each thermometer, temperatures have been computed using a range of pressure values (2, 3, 4, 5 GPa) and for each barometer, pressures have been calculated for a set of temperature values (1000, 1100, 1250, 1400, 1500 °C). Similarly to previous works (Bloch et al., 2017;Weber, 1998 ; Zieman et al., 2023), the *P-T* estimates presented here have been computed considering all iron as Fe^{2+}, although the rock-forming minerals employed for thermobarometry may contain little amounts of Fe^{3+} (Table 2b). A test of the influence of Fe^{3+} on the thermometry of selected peridotite and pyroxenite samples shows that the difference is within a few °C for the Nimis and Taylor (2000), Taylor (1998), Brey and Köhler (1990) calibrations (see also Matjuschkin et al., 2014*)*. Differently, the input of calculated Fe^{3+} in the Harley (1984) geothermometer yields significantly higher estimates, in the order of 100 to 170 °C in pyroxenites, as pointed out by Matjuschkin et al. (2014). The results have been plotted as linear functions in *P-T* diagrams, with red and blue lines representing geothermometers and geobarometers, respectively (Fig. 8). The equilibrium *P-T* values are retrieved through the intersection of the results obtained for the different thermometric and barometric calibrations. The equilibrium *P-T* conditions for all samples are summarized in Fig. 9, with error bars proportional to the area of the domain of intersection of the predictions of the different geothermometer and geobarometers for each sample. Due to the compositional homogeneity of minerals from the different microstructural domains of a single sample, the estimated P-T values for core, rims, and matrix are similar.

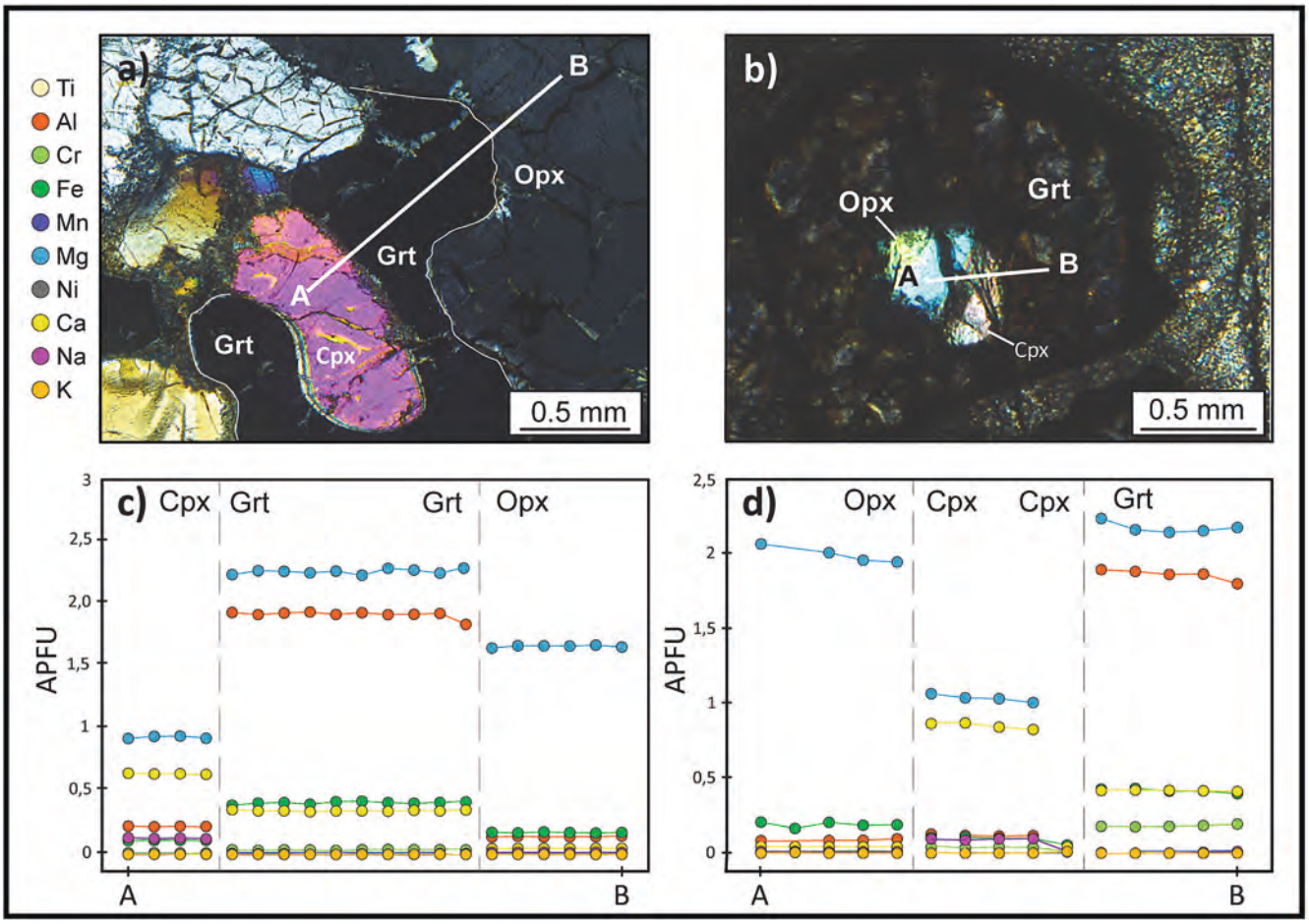

Fig. 6. Results of contiguous WDS analysis – a) Sample COL1 – granular websterite, segment AB indicates analytical profile; b) Sample 18XM3 – mylonitic orthopyroxenite, c) Punctual analysis plot for sample COL1, profile from A to B; d) Punctual analysis plot for sample 18XM3, profile from A to B.

Garnet lherzolites equilibrated at 3.0–3.8 GPa and 1100–1200 °C, with sample 18XM12 recording lower pressures than 18XM4. The spinel lherzolite 18XM5 equilibrated at shallower conditions: 2.2–2.6 GPa and 1100–1190 °C. Garnet websterites equilibrated at 1170–1230 °C and 2.8–3.4 GPa, with comparable results for both samples (COL1 and COL2). The websterite with neither garnet nor spinel equilibrated at *P-T* conditions similar to the garnet websterites, ranging 3 GPa and 1200 °C. However, the estimates for the garnet-free samples should be considered with caution, as in absence of garnet, only the Nimis and Taylor (2000), Taylor (1998), Brey and Köhler (1990) thermometers and the Nimis and Taylor (2000) barometer could be used.

Garnet clinopyroxenites show a wide range of equilibration temperatures and pressures, from 2.4 to 3.7 GPa and 990 to 1140 °C. 18XM11 and 18XM9 equilibrated at comparable conditions: 2.4–3 GPa and 1000–1100 °C for 18XM11 and 2.4–3.3 GPa and 1000–1100 °C for 18XM9. 18XM6 equilibrated at significantly higher P-T conditions (2.6–4 GPa and 1010–1190 °C). Due to the lack of orthopyroxene porphyroclasts, we used the composition of the orthopyroxenes in fine-grained matrix for these P-T calculations. For sample 18XM11 only the Nimis and Taylor (2000) geothermometer and geobarometer could be applied due to the lack of orthopyroxene.

The orthopyroxenites 18XM2 and 18XM3 equilibrated between 1050 and 1210 °C and 2.7–4 GPa. Both samples show comparable pressures and slightly different temperatures, with sample 18XM2 recording higher temperatures (ranging 1100–1210 °C) than 18XM3 (ranging 1050–1150 °C).

To summarize, most xenoliths studied here equilibrated at *P-T* conditions between 2.5 and 4 GPa and 1100–1200 °C (Fig. 9), suggesting that they sample a deep and rather hot domain of the mantle wedge. The garnet lherzolites and the websterites equilibrated at similar *P-T* conditions to those estimated by previous authors (Weber, 1998; Zieman et al., 2023) for these rock types. Lower temperatures, but comparable pressures are recorded by the mylonitic orthopyroxenites, whereas the spinel lherzolite recorded similar temperatures but lower pressures. Two of the garnet clinopyroxenites equilibrated at lower *P-T* conditions. Overall, the estimates achieved for the deepest garnet peridotite and garnet pyroxenite (Fig. 9) compare well with the estimates of Zieman et al. (2023) for their deep, near slab, mantle xenoliths.

7. Discussion

Except for one spinel-bearing peridotite and one websterite, the Mercaderes xenoliths studied here are garnet-bearing peridotites and pyroxenites. They equilibrated at depths between 80 and 145 km underneath the volcanic district of southern Colombia and provide information on the petrological and deformation processes occurred in the deep mantle wedge of an active subduction zone. The studied rocks display considerable heterogeneity in terms of lithotypes, textures, mineral abundance and extent of metasomatic overprint. Moreover, although the xenolith sampling was random, the Mercaderes suite is characterized by a surprisingly high proportion of pyroxenites. The formation of pyroxenites in the mantle can be attributed to the following main processes: crystallization of silicate liquids at mantle depths (e.g., Bodinier et al., 1987; Keshav et al., 2007), mantle refertilization via chemical exchange with circulating silicate liquids (e.g., Borghini et al., 2016; Garrido and Bodinier, 1999; Rampone et al., 2004), recycling of

Table 3
Analyses of the trace element compositions of rock-forming minerals from selected samples of the Mercaderes Xenolith.

a.

	Grt Peridotite 18XM4	18XM4	18XM4	18XM4	18XM4	18XM4	Grt websterite COL1						Grt websterite COL2		
	A301 Cpx c	A302 Cpx r	A404 Opx c	A403 Opx r	A201 Grt c	A202 Grt r	A101 Cpx r	A102 Cpx c	A103 Opx c	A104 Opx r	A301Grt c	A302 Grt r	A102 Cpx	A203Opx	A206grt
Li	1.62	1.87	1.84	<1.01	0.93	<0.87	1.76	1.94	0.82	1.49	<0.57	<0.50	1.17	0.54	0.28
Be	bd	bd	bd	bd	bd	bd	<1.28	1.41	<2.60	<0.56	<1.43	<1.38	bd	bd	bd
Sc	16.26	16.69	4.55	4.59	72.99	65.74	20.28	20.45	8.54	7.86	95.81	92.86	25.53	11.88	112.06
TiO2	0.34	0.34	0.15	0.15	0.36	0.36	0.31	0.32	0.14	0.13	0.28	0.27	1821.68	802.37	1949.74
V	287.38	289.62	86.12	87.65	183.17	174.40	198.66	199.91	85.46	85.42	127.15	125.51	236.38	86.60	171.93
Cr	6424.04	6401.23	2253.56	2360.59	10,911.46	10,321.86	3421.66	3287.91	1840.91	1782.42	4217.90	4301.30	4470.01	1855.22	8001.58
Co	27.02	27.94	60.97	62.53	47.76	46.48	27.83	28.16	60.39	58.85	51.78	47.15	32.50	66.06	56.30
Ni	434.82	456.31	903.37	910.30	84.69	84.43	442.55	459.50	887.19	882.20	100.44	106.83	475.16	851.61	103.52
Zn	16.59	17.74	44.10	46.38	16.98	14.88	16.91	17.50	46.13	44.68	17.35	19.90	20.34	47.21	21.97
Rb	0.02	0.03	<0.0157	<0.0176	<0.037	<0.0197	<0.0171	<0.0193	<0.0221	<0.0158	<0.0238	0.04	0.06	<0.0231	0.03
Sr	82.37	81.96	0.47	0.50	0.15	0.40	72.53	73.04	0.72	0.73	0.29	0.23	121.44	1.20	0.40
Y	2.02	2.07	0.14	0.12	17.18	14.88	4.39	4.64	0.49	0.42	50.36	38.94	2.62	0.27	21.97
Zr	10.16	10.09	0.62	0.57	20.90	20.86	21.06	21.22	2.49	1.92	50.73	54.48	16.01	1.50	48.11
Nb	0.08	0.08	<0.0163	<0.0098	<0.0236	0.08	0.13	0.16	<0.0123	0.01	0.05	0.04	0.05	0.02	0.05
Cs	<0.0066	<0.0063	<0.0056	<0.0105	0.01	<0.0085	<0.0082	0.01	0.01	<0.0073	<0.0090	<0.0078	0.02	<0.0070	<0.0065
Ba	0.09	0.12	0.01	<0.0155	<0.0170	0.02	0.08	0.15	0.01	0.01	<0.0138	<0.0090	0.29	<0.0128	<0.00
La	0.86	0.88	0.01	<0.0087	<0.0092	0.03	2.49	2.30	<0.0106	0.02	0.03	0.02	2.46	0.02	0.03
Ce	3.63	3.73	0.03	0.05	0.12	0.14	7.31	7.67	0.08	0.09	0.23	0.26	9.60	0.10	0.36
Pr	0.59	0.60	<0.0079	<0.0058	0.04	0.06	1.30	1.24	0.02	0.02	0.11	0.12	1.49	0.02	0.10
Nd	4.00	3.83	0.07	0.08	0.36	0.49	6.79	6.98	0.16	0.12	0.89	1.00	7.12	0.10	1.00
Sm	1.17	1.31	<0.051	<0.037	0.57	0.59	1.82	2.11	<0.075	0.05	1.13	1.11	1.58	<0.065	0.72
Eu	0.50	0.48	<0.0174	0.01	0.37	0.39	0.59	0.66	<0.0203	0.02	0.57	0.50	0.50	<0.0144	0.48
Gd	1.01	0.99	<0.032	<0.053	1.46	1.36	1.87	2.24	bd	0.06	2.47	2.29	0.98	<0.057	1.52
Tb	0.13	0.14	<0.0071	<0.0083	0.33	0.28	0.26	0.28	<0.0121	0.01	0.70	0.64	0.12	<0.0053	0.43
Dy	0.70	0.75	<0.029	0.05	2.72	2.34	1.02	1.28	0.06	<0.035	7.08	6.07	0.75	0.08	3.25
Ho	0.09	0.09	<0.0105	0.02	0.65	0.67	0.18	0.19	0.01	0.02	2.00	1.46	0.12	0.02	0.81
Er	0.16	0.15	0.04	0.05	2.41	1.99	0.33	0.37	0.07	<0.033	6.61	4.10	0.25	0.03	2.58
Tm	0.02	0.02		<0.0080	0.40	0.32	0.05	0.04	<0.0129	<0.0091	1.17	0.68	0.02	<0.0051	0.39
Yb	0.08	0.10	<0.045	0.05	3.45	2.50	0.24	0.24	<0.069	0.07	9.36	5.62	0.14	0.04	2.43
Lu	0.01	0.01	0.01	<0.0066	0.47	0.36	0.03	0.04	<0.0141	<0.0081	1.45	0.84	0.01	<0.0054	0.42
Hf	0.54	0.32	<0.027	<0.048	0.40	0.28	0.95	0.92	<0.073	<0.047	1.00	0.85	0.49	0.07	0.85
Ta	0.01	0.01	<0.0071	<0.0090	<0.0154	<0.0066	0.03	0.02	<0.0131	<0.0093	<0.0077	<0.0066	<0.0071	0.01	<0.0070
Pb	0.10	0.14	<0.0168	0.04	0.01	0.04	0.09	0.06	<0.0168	0.06	<0.0148	0.02	0.16	<0.0178	<0.0206
Th	<0.0082	0.02	0.00	<0.0083	<0.0123	<0.0061	0.06	0.07	0.02	<0.0075	0.01	<0.0074	0.03	<0.0067	<0.0126
U	<0.0090	0.01	<0.0085	0.01	<0.0075	0.01	0.01	0.01	0.01	<0.0059	<0.0095	0.01	0.01	0.01	0.02

b.

	Grt cpxenite 18XM6					Grt clinopyroxenite 18XM11					Grt orthopyroxenite 18XM2			Websterite 18XM7	
	A102 Cpx	A103 Grt	A203Grt	A302Cpx	A303Grt	A101 Cpx c	A102 Cpx r	A104 Cpx m	A301 Grt c	A302 Grt r	A102 Cpx	A103 Opx	A105 Grt	A101 Cpx	A103 Opx
Li	0.67	<0.46	<0.50	1.08	1.13	1.61	1.71	1.85	<1.41	<1.61	1.31	1.73	<0.66	1.97	2.66
Be	bd	bd	bd	bd	bd	bd	bd	bd	bd	bd	bd	bd	bd	bd	bd
B	9.98	<5.08	<5.01	7.65	<8.32	11.66	8.39	<6.41	8.52	6.43	25.49	29.39	14.19	<5.51	<6.61
Sc	17.00	61.66	66.17	15.97	63.33	27.57	28.27	31.21	200.79	205.47	15.88	9.49	75.43	38.02	20.86
TiO2	1223.06	1351.48	1419.90	1161.14	1478.63	0.25	0.25	0.26	0.20	0.19	701.05	367.99	1049.70	631.77	376.06
V	191.52	117.63	119.34	184.32	125.06	326.07	319.91	316.46	225.67	225.66	214.89	73.78	178.26	173.84	97.77

(*continued on next page*)

Table 3 (*continued*)

b.

	Grt cpxenite 18XM6					Grt clinopyroxenite 18XM11					Grt orthopyroxenite 18XM2			Websterite 18XM7	
	A102 Cpx	A103 Grt	A203Grt	A302Cpx	A303Grt	A101 Cpx c	A102 Cpx r	A104 Cpx m	A301 Grt c	A302 Grt r	A102 Cpx	A103 Opx	A105 Grt	A101 Cpx	A103 Opx
Cr	2951.56	5322.81	5794.35	2520.56	5253.77	471.28	471.22	431.77	1063.02	1101.45	11,093.27	4068.61	21,604.49	4596.61	3393.96
Co	23.79	44.17	47.13	24.98	45.48	31.75	32.13	33.57	59.94	58.38	29.37	67.32	48.99	27.74	70.49
Ni	496.87	86.60	88.23	491.21	92.04	70.76	70.88	70.79	12.20	13.64	511.23	1016.11	96.17	286.67	638.69
Zn	13.58	15.96	16.08	14.14	14.71	19.95	19.82	21.66	17.65	18.41	24.41	54.50	22.59	18.95	56.89
Rb	<0.056	0.11	0.05	<0.040	<0.085	<0.0148	0.02	<0.057	0.06	0.03	0.19	<0.041	0.21	<0.041	0.05
Sr	86.70	2.21	0.82	85.91	1.447	32.41	33.78	34.61	0.12	0.10	55.54	0.47	0.30	25.01	0.21
Y	1.29	10.21	11.17	1.12	10.21	4.74	5.22	5.84	80.64	84.48	0.32	0.03	3.62	3.58	0.53
Zr	6.13	17.65	18.68	5.8	17.38	2.28	2.31	2.94	7.94	8.27	1.40	0.10	6.14	18.32	0.08
Nb	0.05	0.05	<0.027	0.026	<0.028	0.01	<0.0096	<0.025	<0.0196	0.02	0.02	<0.0151	0.03	<0.0111	<0.0197
Cs	<0.0140	<0.0179	0.02	<0.0129	<0.0244	<0.0034	<0.0054	0.03	0.02	<0.0095	<0.0105	<0.0153	<0.0109	<0.0152	<0.0229
Ba	0.41	0.29	0.03	0.236	0.036	0.01	0.13	0.24	<0.0180	0.08	0.19	0.02	0.40	<0.0156	<0.0129
La	0.89	0.02	<0.0185	0.835	0.029	0.18	0.24	0.20	<0.0100	<0.0153	0.40	0.01	0.04	0.08	0.01
Ce	3.34	0.17	0.12	3.23	0.099	1.01	1.13	0.99	0.03	0.05	1.47	0.03	0.09	0.46	0.02
Pr	0.65	0.05	0.02	0.551	0.031	0.27	0.27	0.31	0.02	<0.0159	0.29	bd	<0.0139	0.12	<0.0144
Nd	3.24	0.31	0.48	3.33	0.294	1.79	2.01	2.18	0.38	0.44	1.44	bd	0.32	0.95	<0.097
Sm	0.98	0.36	0.38	0.941	0.408	0.76	0.84	1.02	0.74	0.68	0.39	<0.062	0.17	0.38	<0.071
Eu	0.35	0.19	0.33	0.308	0.265	0.33	0.36	0.37	0.53	0.48	0.14	<0.0176	0.13	0.19	<0.0202
Gd	0.80	1.08	1.25	0.791	1.018	1.06	1.13	1.30	2.49	2.49	0.30	bd	bd	bd	bd
Tb	0.10	0.26	0.25	0.122	0.216	0.18	0.19	0.22	0.87	0.99	0.03	bd	bd	bd	bd
Dy	0.49	2.02	1.82	0.503	1.8	1.10	1.18	1.31	9.45	8.69	0.13	<0.028	0.83	0.75	bd
Ho	0.07	0.44	0.49	0.06	0.406	0.21	0.24	0.25	2.95	2.98	<0.0074	<0.0088	0.16	0.16	0.02
Er	0.11	1.36	0.97	0.114	1.17	0.43	0.45	0.47	10.17	10.12	0.04	<0.030	0.35	0.38	<0.062
Tm	0.01	0.16	0.17	0.009	0.186	0.05	0.06	0.06	1.65	1.77	bd	bd	bd	bd	< 0.0184
Yb	<0.083	1.15	1.17	<0.060	1.134	0.26	0.32	0.35	12.86	14.13	<0.046	<0.055	0.39	0.45	0.17
Lu	<0.0095	0.15	0.16	<0.0056	0.18	0.03	0.03	bd	2.03	2.22	<0.0087	<0.0089	0.07	0.05	0.02
Hf	0.31	0.33	0.44	0.246	0.305	0.20	0.19	0.28	0.08	0.17	0.09	<0.037	0.10	<0.065	<0.067
Ta	<0.0125	<0.0113	<0.0068	<0.0104	<0.0157	<0.0043	<0.0039	0.02	<0.0107	<0.0081	<0.0088	<0.0094	<0.0117	0.01	<0.0123
Pb	0.25	0.10	0.02	0.134	0.045	bd	<0.051	0.24	<0.030	0.01	0.38	0.51	0.07	0.13	<0.027
Th	<0.0157	0.01	0.00	<0.0144	<0.0273	<0.0063	0.01	<0.0130	<0.0155	<0.0184	<0.0085	<0.0083	<0.0072	<0.0119	<0.0123
U	0.02	<0.0127	0.01	<0.0059	0.014	<0.0050	0.01	<0.029	<0.0152	<0.0114	<0.0091	<0.0077	<0.0116	<0.0111	<0.0196

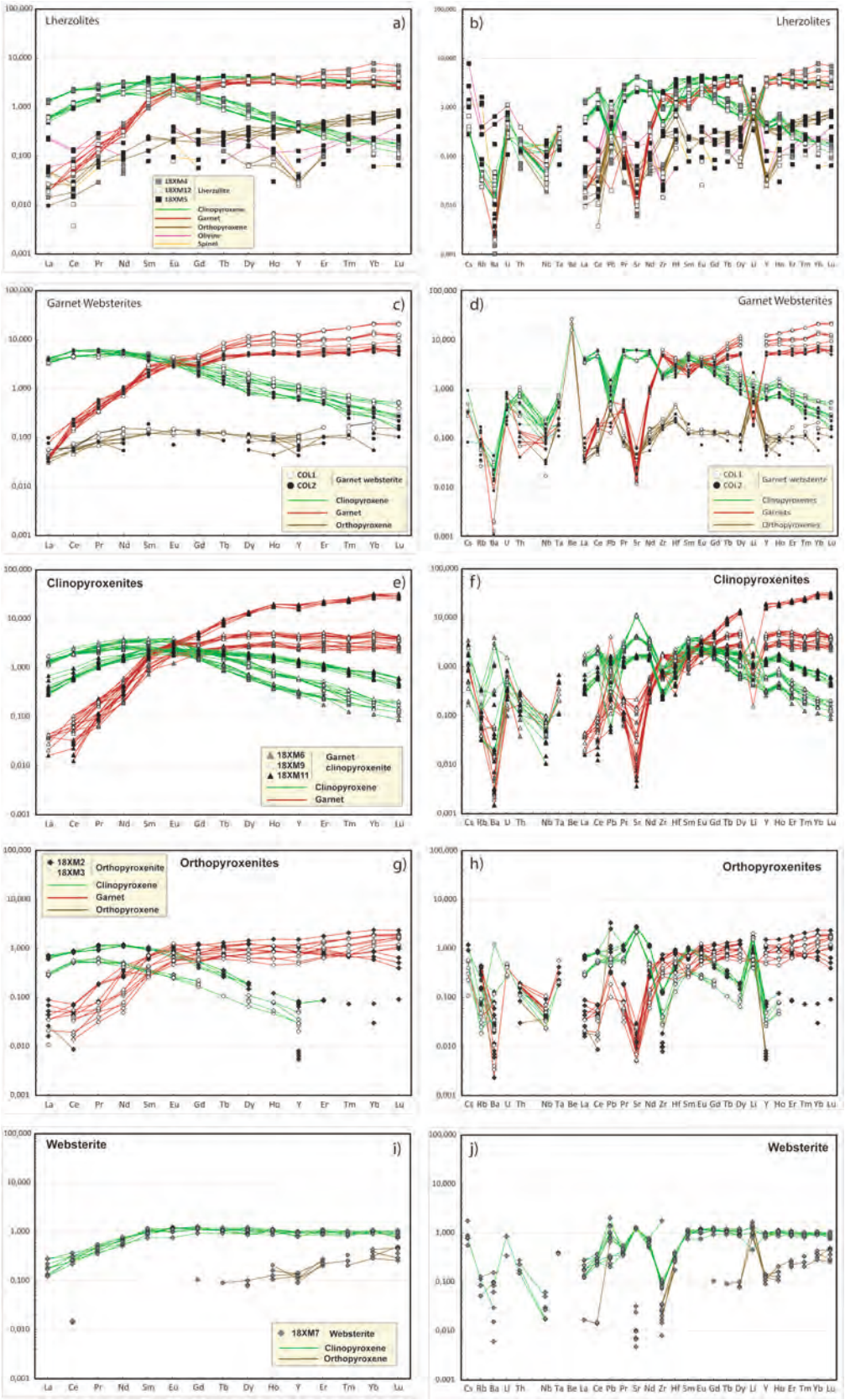

Fig. 7. REE diagrams and Spider Diagrams as result of LA-ICP-MS analysis – a) Lherzolites REE diagram; b) Lherzolites spider diagram; c) Garnet websterites REE diagram; d) Garnet websterites spider diagram; e) Clinopyroxenites REE diagram; f) Clinopyroxenites spider diagram; g) Orthopyroxenites REE diagram; h) Orthopyroxenites spider diagram; i) Websterite REE diagram; j) Websterite spider diagram.

oceanic crusts into the mantle (e.g., Pearson et al., 1991), or sinking of dense deep arc crust into the mantle (Bloch et al., 2017). Hereafter, we discuss the microstructures, mineral assemblages, and metasomatic changes affecting the mantle peridotites and the possible origin of the different pyroxenite types, with the aim of addressing the processes driving the evolution of these deep supra subduction mantle fragments.

Except for a few undeformed samples (e.g., COL1, COL2), the xenolith set presented here were affected by a high stress mylonitic deformation. The (re)crystallization associated to this deformation largely erased the microstructures produced at precursor evolutionary stages. Consequently, these rocks have different microstructures from other supra subduction garnet-bearing mantle peridotites and pyroxenites, which still preserve petrological and textural evidence of a polyphase and colder evolution within the lithosphere of the overriding plate or associated with the subduction-induced flow (e.g., Malaspina et al., 2009; Pellegrino et al., 2021). The present xenoliths were also equilibrated at higher temperatures. Their analysis thus brings light on processes occurring farther from the subducting plate, in the vicinity to the lithosphere to asthenosphere transition in the wedge.

7.1. Lithological heterogeneity and textures

As reported in sections 4 and 5, the Mercaderes mantle xenoliths are heterogeneous in terms of modal composition, texture, and mineral chemistry. Most of them display porphyroclastic textures, with pyroxene and garnet porphyroclasts surrounded by variable volumes of very fine-grained matrix formed by full recrystallization of olivine, when present, and partial recrystallization of orthopyroxene and clinopyroxene (Figs. 2, 3). The extreme grain size refinement (from several millimetres to tens of microns) indicates that the Mercaderes mantle xenoliths were subjected to variable intensities of a high stress-deformation. If the intensity of dynamic recrystallization is used as qualitative proxy for the intensity of the deformation (e.g., Barnhoorn et al., 2004), the lherzolites are in general more deformed than orthopyroxenites, which are more deformed than the websterites and garnet-pyroxenites. This is consistent with the relative strength of the main rock-forming minerals in these rocks, that is, in order of increasing strength: olivine, orthopyroxene, clinopyroxene, and garnet. This high-stress deformation affects all samples, even if it is very weak, only producing undulous extinctions, in the garnet websterites. This implies that this deformation is the last event recorded by the Mercaderes mantle suite before being engaged in the uprising lava. Another line of evidence indicating that this deformation occurred shortly before the fast extraction of xenoliths by the uprising lavas is the preservation of the fine-grained texture in the matrix, which would be quickly erased by static grain growth at the temperatures of 1100–1200 °C at which the xenoliths equilibrated (Furtoss et al., 2021). This deformation is therefore a late and probably punctual event in the history of mantle wedge recorded by the Mercaderes xenoliths. However, the significance and processes at play during this deformation event are not the focus of this study and will be treated in companion paper. In the following paragraphs we focus on the processes that produced the lithological and chemical heterogeneity preceding the deformation event. To do so, we analyse in detail the textures of the least deformed garnet websterite samples COL1 and COL2 and of garnet clinopyroxenite 18XM6, which preserve information on the petrological processes recorded by these rocks.

All three samples are essentially composed of coarse-grained, irregularly shaped crystals; as mentioned above, these rocks are poorly affected by the mylonitic deformation recorded by most Mercaderes mantle samples and show very low volume fractions of fine-grained matrix (Figs. 3 and 4). The EBSD crystal orientation maps highlight that clinopyroxene in sample COL2 and, locally, garnet in sample COL1 have poikilitic habitus, defined by neighboring grains with irregular shapes that share the same crystallographic orientation (Fig. 4b and e). Clinopyroxenes in samples COL1 and 18XM6 are not poikilitic but have clear interstitial habitus. Poikilitic and interstitial habitus can only be formed in a two-phase (solid + liquid) system, by crystallization of a remnant liquid phase in the interstices of an already existing solid grains framework. Alternatively, the coarse deformed and irregularly shaped clinopyroxene crystals from sample COL2 may represent the relics left after partial dissolution and precipitation of orthopyroxene and garnet. In both cases, the preservation of these textures indicates that post-crystallization deformation was small. The pre-deformation textures of the garnet websterites and of the garnet clinopyroxenite 18XM6 may thus be attributed to either crystallization from melts or to melt-rock reaction. The absence of chemical zoning and the homogeneous degree of deformation in minerals (clinopyroxene, orthopyroxene and garnet) do not allow a clear distinction between the two processes.

7.2. Chemical heterogeneity

The textural and petrologic survey of the Mercaderes xenoliths indicates that the uprising magmas sampled a chemically heterogeneous mantle affected by several processes, such as (i) interaction with metasomatic liquids and (ii) recrystallization at depth of lower crustal rocks (Bloch et al., 2017). Here we focus on the main chemical features that highlight the complex sum of chemical processes that modified the mantle section underneath Mercaderes.

7.3. Metasomatism by alkaline melts

The porphyroclastic garnet-peridotite xenoliths 18XM4 and 18XM12 display key differences in their modal (Table 1, Fig. 10), major and trace element mineral and bulk-rock compositions (Figs. 5, 7) suggesting derivation from mantle domains that experienced different extent of reactive interaction with circulating metasomatic melts/liquids. Differently, the high modal amount of orthopyroxene in the spinel peridotite 18XM5 (Table 1) suggests silica influx in this sample, that will be treated in the next section of this discussion section.

Sample 18XM12 displays clinopyroxene abundances of 11% by volume (clinopyroxene/orthopyroxene ratio < 1: Table 1, Fig. 10a); its clinopyroxene has high Mg# and relatively low Na (Fig. 5a) and is depleted in LREE and incompatible elements (Figs. 7a, b). The estimated bulk-rock trace element of 18XM12 (Fig. 11: calculated using the compositions and modal amounts of the rock-forming minerals) is depleted in LREE (Fig. 11a). Overall, this indicates derivation of this sample from a depleted mantle source. Differently, 18XM4 has higher modal clinopyroxene (23% by volume), whose abundance is higher than that of the associated orthopyroxene (12% by volume, clinopyroxene/orthopyroxene ratio ~ 2; Fig. 10b). Moreover, the 18XM4 clinopyroxene has higher Na contents, higher absolute trace element and REE concentrations (Figs. 5, 7). The recalculated bulk rock REE pattern of this sample also shows significant LREE enrichment with respect to garnet peridotite 18XM12 (Fig. 11).

The two garnet-bearing peridotites thus represent deep mantle domains variably affected by interaction with metasomatic agents: 18XM12 derives from a depleted mantle source, while the enrichment in clinopyroxene, LREE and other incompatible trace elements in 18XM4 indicates metasomatism, likely driven by influx of alkaline melts. Considering that in these peridotite samples clinopyroxene occurs as porphyroclast embedded in the foliated matrix, we conclude that metasomatism predated the deformation that produced the grain size refinement.

7.4. Metasomatism by Si-rich liquids

The Mercaderes garnet-orthopyroxenite xenoliths 18XM2 and 18XM3 are rare rock types, with few examples in literature. Orthopyroxene crystallization in mantle rocks has been attributed to the reaction with Si-rich liquids (e.g., Arai and Ishimaru, 2008; Soustelle et al., 2010; Zanetti et al., 1999). As discussed in section 4, the orthopyroxenites 18XM2 and 18XM3 have high Mg# and high Cr contents, indicating

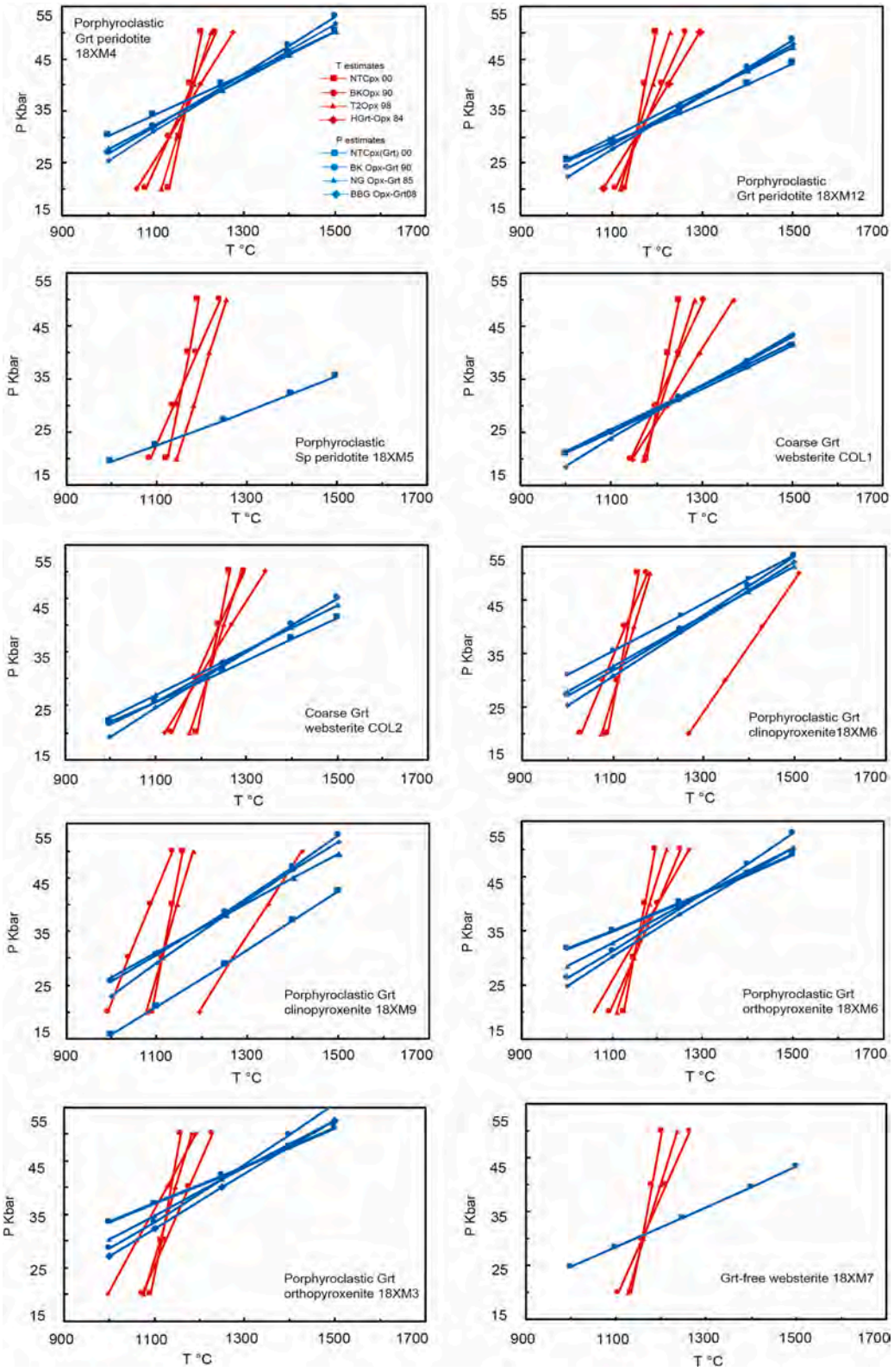

Fig. 8. P-T plots of the utilized Geothermometers (red lines and symbols) and Geobarometers (blue lines and symbols) for each sample. The part highlighted in green represents the selected interval plotted in Fig. 9. Geothermometer (in red) and geobarometers (in blue) employed: NTClinopyroxene00 Nimis and Taylor (2000); BKorthopyroxene90 Brey & Koelher (1990); T2orthopyroxene98 Taylor (1998); Hgarnet-orthopyroxene Harley (1984). Abbreviations for geobarometers: NTclinopyroxene(Garnet)00 Nimis and Taylor (2000); BK orthopyroxene-Garnet90 Brey & Koelher (1990); NG orthopyroxene-garnet85 Nickel and Green (1985); BBG orthopyroxene-garnet08 Brey, Bulatov, Girnis (20087). (For interpretation of the references to colour in this figure legend, the reader is referred to the web version of this article.)

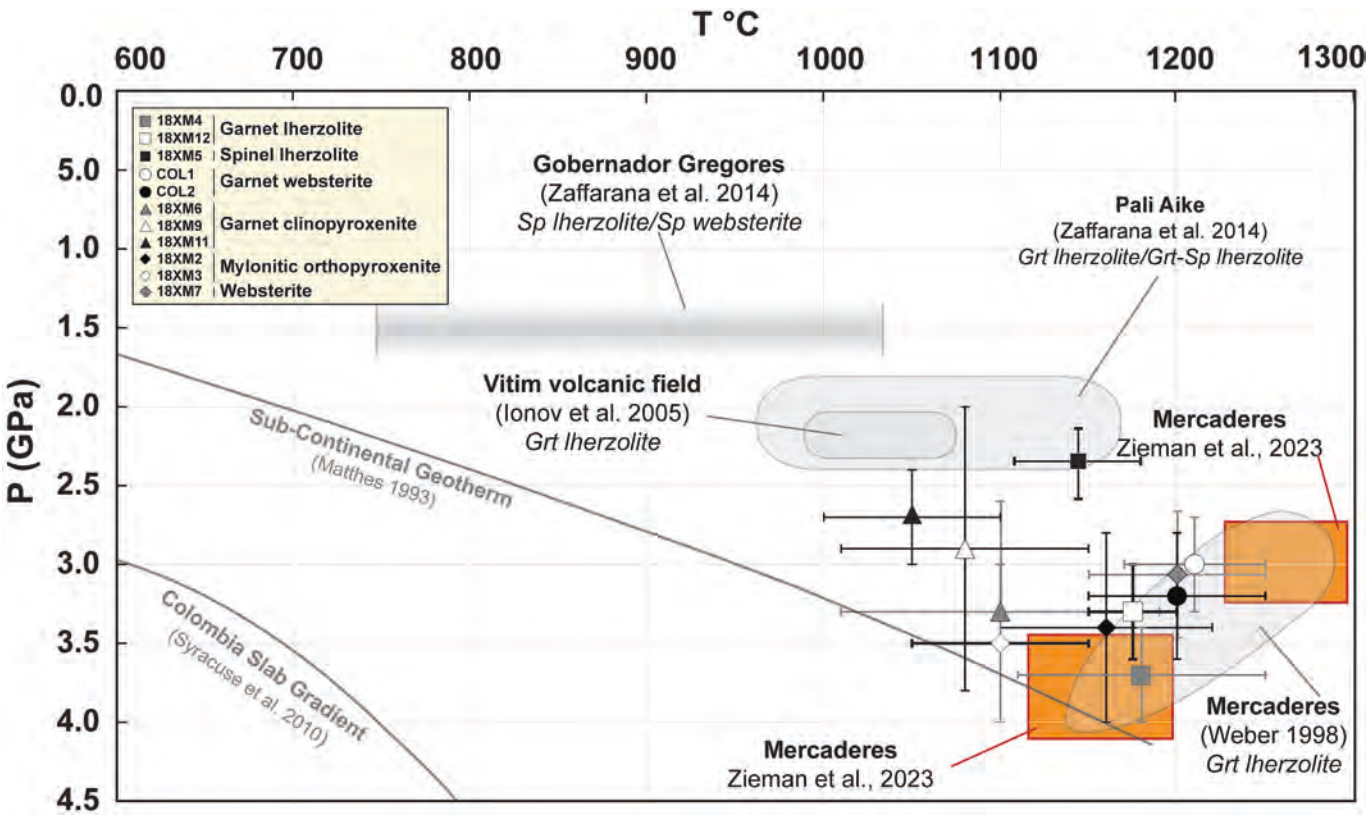

Fig. 9. P-T equilibration estimates of the studied xenolith suite.

significant initial depletion of these rock types which can correspond to residues of partial melting processes. Orthopyroxene crystallization at the expense of a very depleted (olivine-rich) protolith could be due to reaction with Si-rich liquids (unclear if fluids or melts), likely originated by dehydration/melting of the subducting slab. To explain the high Mg# of these garnet-orthopyroxenite samples even after interaction with subduction liquids we speculate that the protoliths were extremely depleted, such as residual dunite with chromitite layers. Interaction of such rocks with slab-derived melts at high pressure conditions might have caused massive crystallization of orthopyroxene (Wang et al., 2016). The positive Pb and Sr anomalies in the spider diagrams (Fig. 7h) support a crustal contribution to the reactive metasomatic agents during melt-rock interaction processes.

Considering the LREE-depleted pattern and the high modal orthopyroxene content of the spinel peridotite 18XM5 (49% olivine, 44% orthopyroxene, 6% clinopyroxene), one may argue that this sample, although derived from a shallower level of the mantle column underneath Mercaderes, experienced a history of element depletion and silica influx similar to that of the garnet orthopyroxenites 18XM2 and 18XM3.

The websterite 18XM7 also shares chemical analogies with garnet-orthopyroxenites 18XM2 and 18XM3, such as the Pb and Sr anomalies (Fig. 7j) and the Si-enriched fingerprint, which point to interaction with subduction melts. Moreover, the REE composition of 18XM7 (Fig. 7i) shows a flat HREE profile for clinopyroxenes, meaning that this rock formed at shallower depths, outside the stability field of garnet, since preferential incorporation of HREE into garnet during crystallization would have induced HREE depletion in clinopyroxene. This evidence suggests that interactions with slab-derived melts not only took place at high depths and close to the slab (forming the above described orthopyroxenites), but also at shallower mantle levels underneath Mercaderes.

To summarize, based on the rock textures and compositions we provide evidence that the studied samples record various episodes/styles of melt-rock interaction in the mantle wedge: (1) garnet peridotites 18XM4 and 18XM12 record variable modification of a depleted mantle possibly by alkaline basaltic melts and garnet websterites COL1 and COL2 retain textural features indicative of partial crystallization of these melts at depths >90 km; (2) the peridotite sample 18XM12 experienced increase in clinopyroxene modal content likely due to interaction with alkali-bearing melts at shallower depths; (3) orthopyroxenites 18XM2, 18XM3 and websterite 18XM7 show high Si contents and anomalies in Pb and Sr, suggesting interaction with metasomatic, slab-derived liquids. In conclusion, the mantle environment sampled by the Mercaderes xenolith suite is characterized by multiple events of melt-rock interaction, different in nature and extent, that produced a compositionally heterogeneus mantle.

7.5. *Crustal delamination and foundering*

The garnet clinopyroxenites 18XM6, 18XM9, 18XM11 studied here, although they have comparable modal composition, display distinct chemical compositions, suggesting that 18XM6 and 18XM9 likely had a different origin and evolution with respect to 18XM11. Fig. 12a reports the bulk Mg# and equilibration depths of our garnet-bearing samples compared to those examined by Bloch et al. (2017) using bulk XMg calculated based on the major element composition of all rock-forming minerals and modal estimates derived from the EBSD maps. Garnet clinopyroxenites 18XM6 and 18XM9 have higher Mg# and record higher recrystallization depths (125–130 km considering 1 GPa ~ 37 km as Bloch et al., 2017) than 18XM11 (~ 100 km). The mantle xenoliths studied here plot on the continuation of the trend identified by Bloch et al. (2017) and Zieman et al. (2023) as representative of deep foundering of sub-crustal slices. It is noteworthy that the deepest equilibrated xenolith from the suite studied by Bloch et al. (2017), which was the sole sample not interpreted as recording crustal foundering, plots along this steeper trend.

The trace element composition of garnet from 18XM6 and 18XM9 and the estimated bulk-rock trace element patterns of these samples

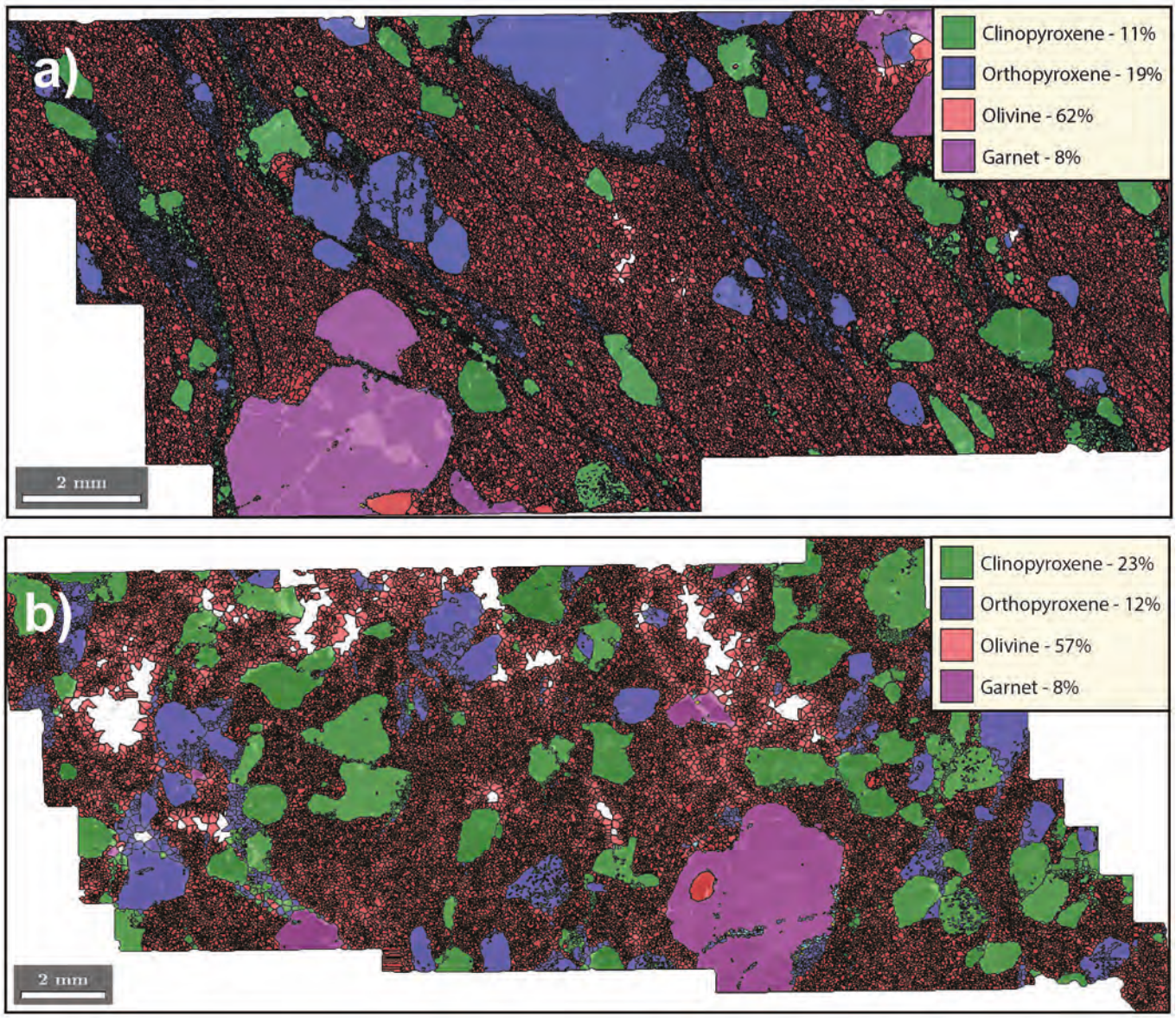

Fig. 10. Modal maps of samples 18XM4 (upper image) and 18XM12 (lower image) obtained through EBSD analysis.

display marked positive Sr anomalies and small Eu anomalies, represented by Eu/Eu* values of 1.2 and 1.3 for 18XM6 and 18XM9, respectively (Fig. 12b). Such anomalies are absent in 18XM11, showing an Eu/Eu* ratio of 1 (Fig. 12b). These features, together with the almost flat MREE-HREE spectra ($Sm_N/Yb_N \sim 1.5$) suggests that 18XM6 and 18XM9 can derive from Mg-rich, plagioclase-bearing (and garnet-absent) low-pressure rocks (i.e., gabbroic cumulates). Their equilibration in the garnet field implies that after crystallization these clinopyroxenites were transported to deeper levels in the mantle. They may therefore record foundering of gabbroic sections formed at the base of the crust, as previously suggested for the Mercaderes area and for larger domains of the Andes (Bloch et al., 2017; DeCelles et al., 2009; Kay and Kay, 1993; Zieman et al., 2023). In terms of rock texture, the garnet clinopyroxenites 18XM9, and to a lesser extent 18XM6, have lost all textural record of their initial low-pressure evolution. The only evidence of a crustal origin of these rocks are their positive Eu and Sr anomalies (Fig. 12b). As an alternative hypothesis, the Sr enrichment recorded by the above garnet pyroxenite xenoliths could also be produced by mantle metasomatic processes. However, the coupled Sr and (minor) Eu anomalies are better interpreted as the record of a former crustal, plagioclase-bearing assembly. In contrast, the absence of Sr and Eu anomalies in 18XM11 ($Sr/Sr^* = 1$ and $Eu/Eu^* = 1.04$, Fig. 7f and 12b) and the significant MREE-HREE fractionation ($SmN/YbN = 0.07$) in this sample suggests that it probably formed at depth as a magmatic garnet-bearing segregate. The low XMg of this garnet clinopyroxenite may be explained if this pyroxenite derived from partial melting of a hybrid mantle source consisting of peridotite with layered eclogite or garnet pyroxenite, as observed in various mantle settings (Borghini et al., 2016; Kogiso et al., 2004; Lambart et al., 2013).

Our results thus reinforce the hypothesis that a foundering process is recorded by part of the Mercaderes high-pressure garnet pyroxenites, which can represent lower crustal rocks that sunk into the mantle down to pressures of 3 to 3.5 GPa or even deeper (Fig. 12a; Bloch et al., 2017). The foundering process recorded by the Mercaderes xenoliths is consistent with larger scale sinking of the Andean arc roots advocated for large sections of the Northern and Central Andes and with the dynamics of orogenic uplift and the associated magmatic, erosional, and sedimentary record (DeCelles et al., 2009; Garzione et al., 2008; Hoorn et al., 2010; Kay and Kay, 1993).

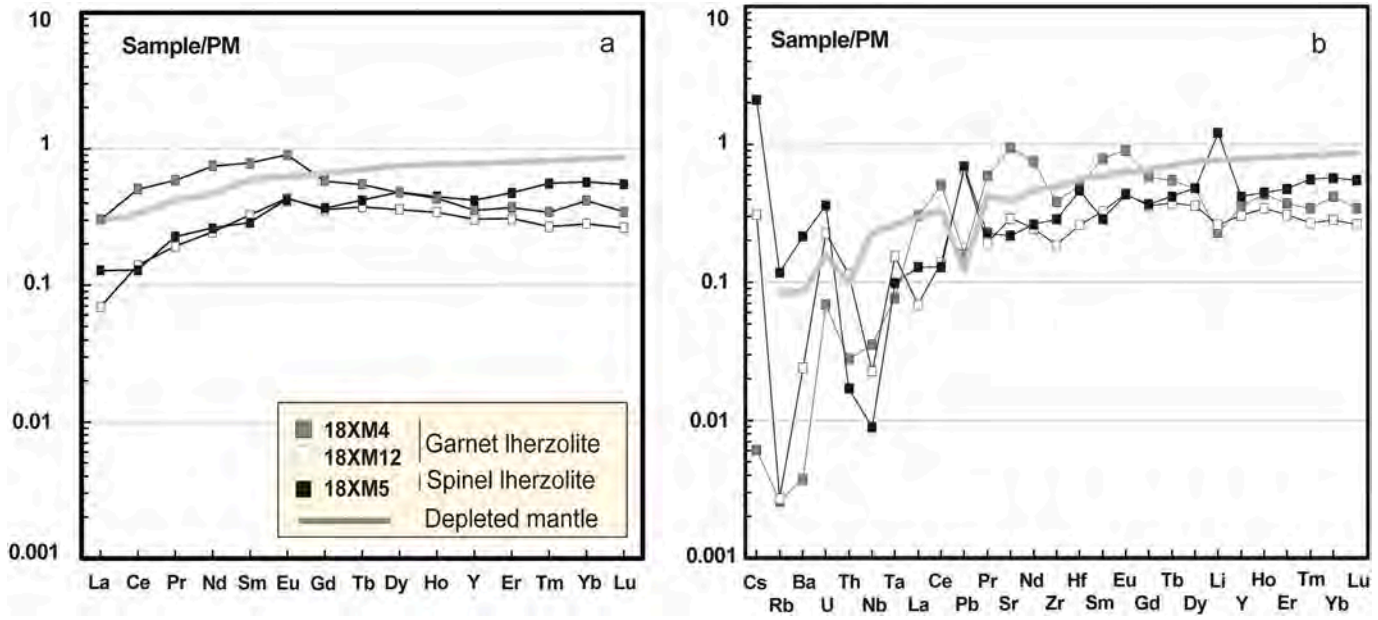

Fig. 11. Calculated, bulk rock REE (a) and trace element (b) composition of the garnet peridotite xenoliths.

7.6. *P-T and evolutionary setting*

The *P-T* estimates for the present set of Mercaderes xenoliths range around 1100–1200 °C and 2.8–4 GPa, with the exception of the spinel peridotite 18XM5 (2.4 GPa-1150 °C). Most samples reported in Fig. 9 thus equilibrated at high temperatures and high pressure conditions: considering the estimate of 1 GPa ~ 37 km depth measured by Bloch et al. (2017) from a set of Mercaderes mantle samples, a Moho depth of 50 km (Mojica Boada et al., 2022; Zieman et al., 2023) and hydrostatic pressure regimes within the mantle column (i.e., in absence of tectonic overpressures), the above pressure values correspond to depths of 110–130 km. The slab underneath Mercaderes being around 120–160 km depth (Wagner et al., 2017), the xenolith set presented here probes a large depth column in the mantle wedge above the subducting Nazca plate, with some of these xenoliths arising from near slab depths, as suggested by Zieman et al. (2023). The temperature estimates presented here (Fig. 9; see also Weber et al., 2002, Rodriguez-Vargas et al., 2005; Bloch et al., 2017) are much higher than the 600–850 °C slab surface temperatures suggested by the available thermal models for the subducting Nazca plate (Syracuse et al., 2016), suggesting that this is a relatively hot supra-subduction mantle.

Our study shows that the Mercaderes xenoliths sampled a very dynamic mantle domain recording a large variety of magmatic processes. Most mantle rocks from Mercaderes (garnet peridotite, garnet websterite and garnet orthopyroxenite) retain the chemical and textural evidence of strong depletion followed by episodes of rock interaction with melts and Si-rich fluids, overprinted by incipient to well-developed mylonite fabrics. In this mantle domain, episodic circulation and chemical interaction of liquids with rocks are thus active processes leading to alkali- and silica-enrichment of the mantle rocks. Two of the garnet clinopyroxenites also provide chemical evidence for foundering of slices of the Colombian arc root. In summary, the Mercaderes

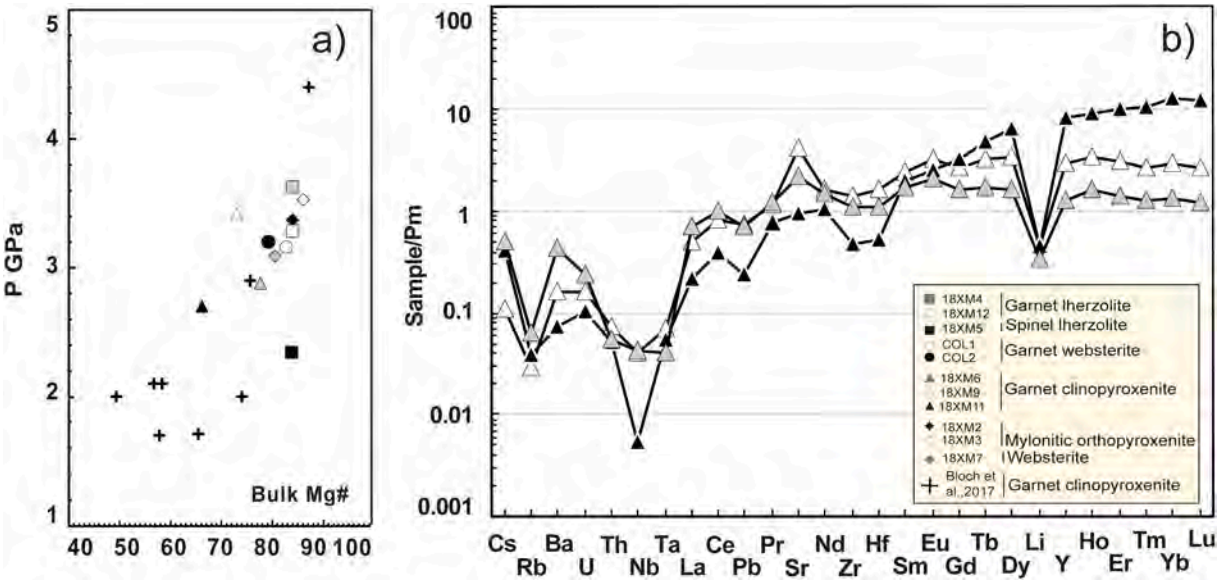

Fig. 12. Reconstructed bulk trace elements compositions for Lherzolites. a) Bulk XMg and b) bulk trace element pattern of the xenolith set presented here (symbols as in plate b) and in Bloch et al. (2017).

xenoliths probe an extremely heterogeneous and chemically active domain of the Colombian mantle wedge, where deep sinking lower crustal rocks, melt metasomatism by distinct venues of chemically different melts, and deformation predated the fast xenolith uprise to the surface.

Declaration of Competing Interest

The authors declare that they have no known competing financial interests or personal relationships that could have appeared to influence the work reported in this paper.

Acknowledgements

We thank Mauricio Ibañez-Mejia and an anonymous referee for critical constructive reviews, Donato Belmonte for scientific discussions and Nadia Malaspina for careful editorial handling.. MS, ER, LN acknowledge funding by the Italian Ministry of University and Research MUR for funding the PRIN COFIN project *Dynastars* (The dynamic mass transfer from slabs to arcs; project n. 2017ZE49E7). AZ acknowledges funding by the Italian Ministry of University and Research MUR for funding the project PRIN 2017 *Micro to Macro - How to unravel the nature of the large magmatic events*. FF and ARV acknowledge the assistance of don Gerardo and don Pedro during field work in Colombia and doña Concha for her lovely lunches.

Appendix A. Supplementary data

Supplementary data to this article can be found online at https://doi.org/10.1016/j.lithos.2023.107401.

References

Arai, S., Ishimaru, S., 2008. Insights into petrological characteristics of the lithosphere of mantle wedge beneath arcs through peridotite xenoliths: a review. J. Petrol. 49, 665–695.

Barnhoorn, A., Bystricky, M., Burlini, L. Kunze, K., 2004. The role of recrystallisation on the deformation behaviour of calcite rocks: large strain torsion experiments on Carrara marble. J. Struct. Geol. 26, 885–903.

Bertotto, G.W., Mazzucchelli, M., Zanetti, A., Vannucci, R., 2013. Petrology and geochemistry of the back-arc lithospheric mantle beneath eastern Payunia (La Pampa, Argentina): evidence from Agua Poca peridotite xenoliths. Geochem. J. 47 (2), 219–234.

Beyer, C., Frost, D.J., Miyajima, N., 2015. Experimental calibration of a garnet–clinopyroxene geobarometer for mantle eclogites. Contrib. Mineral. Petrol. 169, 1–21.

Blanco, J.F., Vargas, C.A., Monsalve, G., 2017. Lithospheric thickness estimation beneath northwestern South America from an S-wavereceiver function analysis. Geochem. Geophys. Geosys. 18 (4), 1376–1387. https://doi.org/10.1002/2016GC006785.

Bloch, E., Ibañez-Mejia, M., Murray, K., Vervoort, J., Müntener, O., 2017. Recent crustal foundering in the Northern Volcanic Zone of the Andean arc: Petrological insights from the roots of a modern subduction zone. Earth Planet. Sci. Lett. 476, 47–58.

Bodinier, J.L., Godard, M., 2003. Orogenic, ophiolitic, and abyssal peridotites. Treatise on geochemistry 2, 568.

Bodinier, J.-L., Guiraud, M., Fabries, J., Dostal, J., Dupuy, C., 1987. Petrogenesis of layered pyroxenites from the Lherz, Freychinede and Prades ultramafic bodies (Ariege, French Pyrenees). Geochim. Cosmochim. Acta 51, 279–290.

Borghini, G., Rampone, E., Zanetti, A., Class, C., Cipriani, A., Hofmann, A.W., Goldstein, S.L., 2016. Pyroxenite layers in the northern Apennines'upper mantle (Italy) - Generation by pyroxenite melting and melt infiltration. J. Petrol. 57-4, 625–653.

Brey, G.P., Köhler, T., 1990. Geothermobarometry in four-phase lherzolites II. New thermobarometers, and practical assessment of existing thermobarometers. J. Petrol. 31 (6), 1353–1378.

Brey, G.P., Bulatov, V.K., Girnis, A.V., 2008. Geobarometry for peridotites: experiments in simple and natural systems from 6 to 10 GPa. J. Petrol. 49 (1), 3–24.

Brueckner, H.K., Medaris, L.G., 2000. A general model for the intrusion and evolution of 'mantle'garnet peridotites in high-pressure and ultra-high-pressure metamorphic terranes. J. Metam. Geol. 18 (2), 123–133.

Cartigny, P., Marty, B., 2013. Nitrogen isotopes and mantle geodynamics: the emergence of life and the atmosphere–crust–mantle connection. Elements 9 (5), 359–366.

Comin-Chiaramonti, P., Antonini, P., Girardi, V.A.V., Gomes, C.B., Laurora, S., Zanetti, A., 2001. Mantle Xenoliths from Ñemby, Eastern Paraguay: O-Sr-Nd isotopes and trace elements of hosted clinopyroxenes.

Currie, C.A., Ducea, M.N., DeCelles, P.G., Beaumont, C., Carrapa, B., Kapp, P.A., 2015. Geodynamic models of Cordilleran orogens: Gravitational instability of magmatic arc roots. Geol. Soc. Am. Mem. 212, 1–22.

Dantas, C., 2007. Caractérisation du manteau supérieur patagonien: les enclaves ultramafiques et mafiques dans les laves alcalines (Doctoral dissertation,. Université Paul Sabatier-Toulouse III.

Dasgupta, R., 2013. Ingassing, storage, and outgassing of terrestrial carbon through geologic time. Rev. Mineral. Geochem. 75 (1), 183–229.

DeCelles, P.G., Ducea, M.N., Kapp, P., Zandt, G., 2009. Cyclicity in Cordilleran orogenic systems. Nat. Geosci. 2 (4), 251–257.

Droop, G.T.R., 1987. A general equation for estimating Fe 3+concentrations in ferromagnesian silicates and oxides from microprobe analyses, using stoichiometric criteria. Mineral. Mag. 51, 431–435.

Ferri, F., Poli, S., Rodriguez-Vargas, A., 2017. Andean Volcanoes Record Carbonatite Mantle Metasomatism and CO2 Degassing at Subduction zones. Goldschmidt conference 2017.

Furtoss, J., Petit, C., Tommasi, A., Ganino, C., Piño-Munoz, D., Bernacki, M., 2021. On the role of solute drag in reconciling laboratory and natural constraints on olivine grain growth kinetics. Geophys. J. Intern. 224, 1360–1370.

Ganguly, J., Cheng, W., Tirone, M., 1996. Thermodynamics of aluminosilicate garnet solid solution: new experimental data, an optimized model, and thermometric applications. Contrib. Mineral. Petrol. 126, 137–151.

Garrido, C.J., Bodinier, J.L., 1999. Diversity of mafic rocks in the Ronda peridotite: evidence for pervasive melt–rock reaction during heating of subcontinental lithosphere by upwelling asthenosphere. J. Petrol. 40, 729–754.

Garzione, C.N., Hoke, G.D., Libarkin, J.C., Withers, S., MacFadden, B., Eiler, J., et al., 2008. Rise of the Andes. Science 320 (5881), 1304–1307.

Gianola, O., Costa, B., Ferri, F., Gilio, M., Petrelli, M., Murri, M., Alvaro, M., Rodríguez-Vargas, A., Poli, S., Cesare, B., 2023. Melt Inclusions in Arclogitic Xenoliths Constrain the Genesis of the Lower Continental Arc Crust beneath the Northern Volcanic Zone, Colombia. J. Pet. 64 (6), 1–24. https://doi.org/10.1093/petrology/egad038.

Godard, G., Martin, S., Prosser, G., Kienast, J.R., Morten, L., 1996. Variscan migmatites, eclogites and garnet-peridotites of the Ulten zone, Eastern Austroalpine system. Tectonophysics 259 (4), 313–341.

Grégoire, M., McInnes, B.I., O'Reilly, S.Y., 2001. Hydrous metasomatism of oceanic sub-arc mantle, Lihir, Papua New Guinea Part 2. Trace element characteristics of slab-derived fluids. Lithos 59, 91–108.

Grohn, Lisa J., Ibañe-Mejía, M., 2018. Fingerprinting Crustal Foundering in the Northern Andean Volcanic Zone Using Basalt Geochemistry, GSA Annual Meeting in Indianapolis, Indiana.

Grove, T.L., Chatterjee, N., Parman, S.W., MÚdard, E., 2006. The influence of H2O on mantle wedge melting. Earth Planet. Sci. Lett. 249 (1–2), 74–89.

Gudelius, D., Aulbach, S., Braga, R., Hofer, H.E., Woodland, A.B., Gerdes, A., 2019. (2019) Element transfer and Redox Conditions in Continental Subduction zones: New Insights from Peridotites of the Ulten Zone, North Italy. J. Petrol. 60 (2), 231–268.

Harley, S.L., 1984. An experimental study of the partitioning of Fe and Mg between garnet and orthopyroxene. Contrib. Mineral. Petrol. 86 (4), 359–373.

Hoorn, C., Wesselingh, F.P., Ter Steege, H., Bermudez, M.A., Mora, A., Sevink, J., Antonelli, A., 2010. Amazonia through time: Andean uplift, climate change, landscape evolution, and biodiversity. Science 330 (6006), 927–931.

Ionov, D.A., Bigot, F., Braga, R., 2017. The provenance of the lithospheric mantle in continental collision zones: petrology and geochemistry of peridotites in the Ulten–Nonsberg Zone (Eastern Alps). J. Petrol. 58, 1451–1472.

Kay, R.W., Kay, S.M., 1993. Delamination and delamination magmatism. Tectonophysics 219 (1–3), 177–189.

Keshav, S., Sen, G., Presnall, D.C., 2007. Garnet-bearing xenoliths from Salt Lake Crater, Oahu, Hawaii: high-pressure fractional crystallization in the oceanic mantle. J. Petrol. 48, 1681–1724.

Kogiso, T., Hirschmann, M.M., Reiners, W., 2004. Length scales of mantle heterogeneities and their relationship to ocean island basalt geochemistry. Geochim. Cosmochim. Acta 68, 345–360.

Lambart, S., Laporte, D., Schiano, P., 2013. Markers of the pyroxenite contribution in the major-element compositions of oceanic basalts: Review of the experimental constraints. Lithos 160–161, 14–36.

Laurora, A., Mazzucchelli, M., Rivalenti, G., Vannucci, R., Zanetti, A., Barbieri, M.A., Cingolani, C.A., 2001. Metasomatism and melting in carbonated peridotite xenoliths from the mantle wedge: the Gobernador Gregores case (Southern Patagonia). J. Petrol. 42 (1), 69–87.

Locock, A.J., 2008. An Excel spreadsheet to recast analyses of garnet into end-member components, and a synopsis of the crystal chemistry of natural silicate garnets. Comput. Geosci. 34, 1769–1780.

Malaspina, N., Hermann, J., Scambelluri, M., 2009. Fluid/mineral interaction in UHP garnet peridotite. Lithos 107, 38–52.

Malaspina, N., Langenhorst, F., Fumagalli, P., Tumiati, S., Poli, S., 2012. Fe3. Distribution between garnet and pyroxenes in mantle wedge carbonate-bearing garnet peridotites (Sulu, China) and implications for their oxidation state. Lithos 146–147, 11–17.

Matjuschkin, V., Brey, G.P., Hofer, H.E., Woodland, A.B., 2014. The influence of Fe3+ on garnet–orthopyroxene and garnet–olivine geothermometers. Contrib. Mineral. Petrol. 167, 972.

McDonough, W.F., Sun, S.S., 1995. The composition of the Earth. Chem. Geol. 120 (3–4), 223–253.

McInnes, B.I., Grégoire, M., Binns, R.A., Herzig, P.M., Hannington, M.D., 2001. Hydrous metasomatism of oceanic sub-arc mantle, Lihir, Papua New Guinea: petrology and

geochemistry of fluid-metasomatised mantle wedge xenoliths. Earth Planet. Sci. Lett. 188, 169–183.
Miller, C., Zanetti, A., Thöni, M., Konzett, J., 2007. Eclogitisation of gabbroic rocks: Redistribution of trace elements and Zr in rutile thermometry in an Eo-Alpine subduction zone (Eastern Alps). Chem. Geol. 239, 96–123. https://doi.org/10.1016/j.chemgeo.2007.01.001.
Mojica Boada, M.J., Poveda, E., Tary, J.B., 2022. Lithospheric and slab configurations from receiver function imaging in northwestern South America, Colombia. Journal of Geophysical Research: Solid. Earth 127 (e2022JB024475).
Nickel, K.G., Green, D.H., 1985. Empirical geothermobarometry for garnet peridotites and implications for the nature of the lithosphere, kimberlites and diamonds. Earth Planet. Sci. Lett. 73 (1), 158–170.
Nimis, P., Taylor, W.R., 2000. Single clinopyroxene thermobarometry for garnet peridotites. Part I. Calibration and testing of a Cr-in-Clinopyroxene barometer and an enstatite-in-Clinopyroxene thermometer. Contrib. Mineral. Petrol. 139, 541–554.
Pardo, N., Pulgarín, B., Betancourt, V., Lucchi, F., Valencia, L.J., 2019. Facing geological mapping at low-latitude volcanoes: the Doña JuanaVolcanic complex study-case, SW-Colombia. Journal of Volcanology and Geothermal Research 385, 46–67.
Pearson, D.G., Davies, G.R., Nixon, P.H., Greenwood, P.B., Mattey, D.P., 1991. Oxygen isotope evidence for the origin of pyroxenites in the Beni Boussera peridotite massif, North Morocco: derivation from subducted oceanic lithosphere. Earth Planet. Sci. Lett. 102, 289–301.
Pellegrino, L., Menegon, L., Zanchetta, S., Lagenhorst, F., Pollock, K., Tumiati, S., Malaspina, N., 2021. Reaction-induced mantle weakening at high-pressure conditions: an example from garnet pyroxenites of Ulten Zone (Eastern Alps, N Italy). J. Geophys. Res. Solid Earth 126, 1–23. https://doi.org/10.1029/2021JB022584 e2021JB022584.
Ponce, A.D., Bertotto, G.W., Zanetti, A., Brunelli, D., Giovanardi, T., Aragón, E., Mazzucchelli, M., et al., 2015. Short-scale variability of the SCLM beneath the extra-Andeanback-arc (Paso de Indios, Argentina): evidence from spinel-faciesmantle xenoliths. Open Geosciences 7 (1).
Rampone, E., Morten, L., 2001. Records of crustal metasomatism in the garnet peridotites of the Ulten Zone (Upper Austroalpine, Eastern Alps). J. Petrol. 42 (1), 207–219.
Rampone, E., Romairone, A., Hofmann, A.W., 2004. Contrasting bulk and mineral chemistry in depleted peridotites: evidence for reactive porous flow. Earth Planet. Sci. Lett. 218, 491–506.
Rivalenti, G., Mazzucchelli, M., Girardi, V.A., Vannucci, R., Barbieri, M.A., Zanetti, A., Goldstein, S.L., 2000. Composition and processes of the mantle lithosphere in northeastern Brazil and Fernando de Noronha: evidence from mantle xenoliths. Contrib. Mineral. Petrol. 138, 308–325.
Rivalenti, G., Zanetti, A., Mazzucchelli, M., Vannucci, R., Cingolani, C.A., 2004. Equivocal carbonatite markers in the mantle xenoliths of the Patagonia backarc: the Gobernador Gregores case (Santa Cruz Province, Argentina). Contrib. Mineral. Petrol. 147, 647–670.
Rivalenti, G., Mazzucchelli, M., Zanetti, A., Vannucci, R., Bollinger, C., Hémond, C., Bertotto, G.W., 2007. Xenoliths from Cerro de los Chenques (Patagonia): an example of slab-related metasomatism in the backarc lithospheric mantle. Lithos 99 (1–2), 45–67.
Rodriguez-Vargas, A., Koester, E., Mallmann, G., Conceição, R.V., Kawashita, K., Weber, M.B.I., 2005. Mantle diversity beneath the Colombian Andes, northern volcanic zone: constraints from Sr and Nd Isotopes. Lithos 82 (3–4), 471–484.
Sapienza, G.T., Scambelluri, M., Braga, R., 2009. Dolomite-bearing orogenic garnet peridotites witness fluid-mediated carbon recycling in a mantle wedge (Ulten Zone, Eastern Alps, Italy). Contrib. Mineral. Petrol. 158, 401–420.
Scambelluri, M., Hermann, J., Morten, L., Rampone, E., 2006. Melt-versus fluid-induced metasomatism in spinel to garnet wedge peridotites (Ulten Zone, Eastern Italian Alps): clues from trace element and Li abundances. Contrib. Mineral. Petrol. 151, 372–394.
Scambelluri, M., Pettke, T., Van Roermund, H.L.M., 2008. Majoritic garnets monitor deep subduction fluid flow and mantle dynamics. Geology 36, 59–62.
Scambelluri, M., Van Roermund, H.L., Pettke, T., 2010. Mantle wedge peridotites: fossil reservoirs of deep subduction zone processes: inferences from high and ultrahigh-pressure rocks from Bardane (Western Norway) and Ulten (Italian Alps). Lithos 120 (1–2), 186–201.
Soustelle, V., Tommasi, A., Demouchy, S., Ionov, D., 2010. Deformation and fluid-rock interactions in the supra-subduction mantle: Microstructures and water contents in peridotite xenoliths from the Avacha Volcano, Kamchatka. J. Petrol. 51, 363–394.
Stern, R.J., 2002. Subduction zones. Rev. Geophys. 40 (4) (3–1).
Sun, M., Bezada, M.J., Cornthwaite, J., Prieto, G.A., Niu, F., Levander, A., 2022. Overlapping slabs: Untangling subduction in NW South America through finite-frequency teleseismic tomography. Earth Planet. Sci. Lett. 577, 117253 https://doi.org/10.1016/j.
Syracuse, E.M., Maceira, M., Prieto, G.A., Zhang, H., Ammon, C.J., 2016. Multiple plates subducting beneath Colombia, as illuminated by seismicity and velocity from the joint inversion of seismic and gravity data. Earth Planet. Sci. Lett. 444, 139–149.
Tatsumi, Y., Stern, R.J., 2006. Factory. Oceanography 19 (4), 104.
Tatsumi, Y., Sakuyama, M., Fukuyama, H., Kushiro, I., 1983. Generation of arc basalt magmas and thermal structure of the mantle wedge in subduction zones. J. Geophys. Res. Solid Earth 88 (B7), 5815–5825.
Taylor, W.R., 1998. An experimental test of some geothermometer and geobaro-meter formulations for upper mantle peridotites with application to the ther-mobarometry of fertile lherzolite and garnet websterite. Neues Jahrbuch für Mineralogie-Abhandlungen 381–408.
Tumiati, S., Thoni, M., Nimis, P., Martin, S., Mair, V., 2003. Mantle–crust interactions during Variscan subduction in the Eastern Alps (Nonsberg–Ulten zone): geochronology and new petrological constraints. Earth Planet. Sci. Lett. 210, 509–526.
van Keken, P.E., 2003. The structure and dynamics of the mantle wedge. Earth Planet. Sci. Lett. 215 (3–4), 323–338.
Van Roermund, H.L.M., Drury, M.R., 1998. Ultrahigh pressure (P>6Gpa) garnet peridotites in western Norway: Exhumation of mantle rocks from more than 185 km. Terra Nova 10, 295–301.
Van Roermund, H.L.M., Carswell, D.A., Drury, M.R., Heijboer, T.C., 2002. Micro diamonds in a megacrystic garnet websterite pod from Bardane on the island of Fjørtoft, western Norway: evidence for diamond formation in mantle rocks during continental subduction. Geology 30, 959–962.
Wagner, L.S., Jaramillo, J.S., Ramírez-Hoyos, L.F., Monsalve, G., Cardona, A., Becker, T. W., 2017. Transient slab flattening beneath Colombia. Geophys. Res. Lett. 44 (13), 6616–6623.
Wang, C., Liang, Y., Dygert, N., Xu, W., 2016. Formation of orthopyroxenite by reaction between peridotite and hydrous basaltic melt: an experimental study. Contrib. Mineral. Petrol. 171, 77.
Weber, M.B., 1998. The Mercaderes-Rio Mayo xenoliths. In: Colombia: Their Bearing on Mantle and Crustal Processes in the Northern Andes. University of Leicester, United Kingdom.
Weber, M.B., Tarney, J., Kempton, P.D., Kent, R.W., 2002. Crustal make-up of the northern Andes: evidence based on deep crustal xenolith suites, Mercaderes, SW Colombia. Tectonophysics 345 (1–4), 49–82.
Zaffarana, C., Tommasi, A., Vauchez, A., Grégoire, M., 2014. Microstructures and seismic properties of south Patagonian mantle xenoliths (Gobernador Gregores and Pali Aike). Tectonophysics 621, 175–197.
Zanetti, A., Mazzucchelli, M., Rivalenti, G., Vannucci, R., 1999. The Finero phlogopite–peridotite massif: an example of subduction-related metasomatism. Contrib. Mineral. Petrol. 134, 107–122.
Zheng, J.P., Zhang, R.Y., Griffin, W.L., Liou, J.G., O'Reilly, S.Y., 2005. Heterogeneous and metasomatized mantle recorded by trace elements in minerals of the Donghai garnet peridotites, Sulu UHP terrane, China. Chemical Geology 221 (3–4), 243–259.
Zheng, J.P., Sun, M., Griffin, W.L., Zhou, M.F., Zhao, G.C., Robinson, P., Zhang, Z.H., 2008. Age and geochemistry of contrasting peridotite types in the Dabie UHP belt, eastern China: Petrogenetic and geodynamic implications. Chem. Geol. 247 (1–2), 282–304.
Zieman, L., Ibañez-Mejia, M., Rooney, A.D., Bloch, E., Pardo, N., Schoene, B., SzymanowskiD., 2023. To sink, or not to sink: the thermal and density structure of the modern northern Andean arc constrained by xenolith petrology. Geology 51. https://doi.org/10.1130/G50973.1.